10/2-12-90 DS (1)

SANDIA REPORT

SAND89—2535 • UC—406
Unlimited Release
Printed December 1989

Computational and Experimental Analysis of Railgun Structural Performance

G. W. Wellman

Prepared by
Sandia National Laboratories
Albuquerque, New Mexico 87185 and Livermore, California 94550
for the United States Department of Energy
under Contract DE-AC04-76DP00789

Issued by Sandia National Laboratories, operated for the United States Department of Energy by Sandia Corporation.

Available to DOE and DOE contractors from
Office of Scientific and Technical Information
PO Box 62
Oak Ridge, TN 37831

Prices available from (615) 576-8401, FTS 626-8401

Available to the public from
National Technical Information Service
US Department of Commerce
5285 Port Royal Rd
Springfield, VA 22161

NTIS price codes
Printed copy: A04
Microfiche copy: A01

SAND89-2535
Unlimited Release
Printed December 1989

SAND--89-2535

DE90 006418

Computational and Experimental Analysis of Railgun Structural Performance [1]

G. W. Wellman
Applied Mechanics Division I
Sandia National Laboratories
Albuquerque, New Mexico 87185

Abstract

The structural response of plasma armature railguns to the electromagnetic loads imposed during operation has a significant affect on performance. The railgun support structure must minimize bore deformation; thus stiffness and strength are important design parameters. The step by step evolution of the design toward a structure which will tolerate operation with 500 to 700 kA rail currents is presented. The design effort started with the traditional rail/insulator core structure contained within a V-block which provides a preload. Non-linear dynamic analyses together with model tests were used to assess the effects of changes in geometry, materials, and preload on the railgun structural performance.

[1]Prepared by Sandia National Laboratories, New Mexico 87185 and Livermore, California 94550 for the United States Department of Energy under Contract DE-AC04-76DP00789.

Acknowledgments

The author is grateful to David Hannum of the rock mechanics laboratory and Rod May and Larry Dorrell of the experimental mechanics department for the development and performance of the short section model testing. Helpful advice from Allan Susoeff of Lawrence Livermore National Laboratory and the entire staff of the Starfire Project was appreciated.

Contents

Tables

Figures

1. Introduction

A plasma armature railgun is being designed to accelerate small projectiles (3 g mass) to 15 km/s, a velocity much higher than achievable with current light gas gun technology. Projectiles at these velocities, upon impact with a target plate, produce the high temperatures and pressures required for equation-of-state studies [1]. The gun rails are connected to an electrical current source (capacitor banks). A plasma armature is formed behind the nonconducting projectile between two conducting rails to complete the electrical circuit. This plasma armature is accelerated down the gun barrel by the magnetic fields generated by the electric currents in the rails. The plasma forces can be defined in terms of either armature current density and rail magnetic flux density ($\mathbf{J} \times \mathbf{B}$) or rail inductance gradient and armature current ($L' I^2$). These forces push on the tail of the projectile, accelerating it down the gun bore. Higher projectile velocities can be attained because the plasma velocity is not limited to the speed of sound of the driving gas as is the case for conventional powder or gas guns.

The railgun geometry considered here consists of a single pair of conducting rails separated by a pair of insulating bore liners held in place by a set of insulating supports. The rails and insulating supports are confined within a set of bolted steel V-blocks. A typical railgun structure is shown in cross-section in Figure 1.1.

The plasma pressure in the gun bore along with the magnetic loads on the rails tend to force the rails to separate. The railgun structure must provide sufficient strength to resist these operating loads. In addition, the railgun performance is affected by bore deformations. Excessive bore deformation leads to plasma blow-by and the potential for subsequent arcing between the rails ahead of the projectile. The formation of gaps between the rails and the insulating supports also allows contaminants to be trapped. These contaminants can provide electrical current paths which prevent the gun from being refired until extensive disassembly and cleaning is performed. Therefore, the railgun structure must minimize bore deformations in addition to providing the required strength to resist the operating loads.

In practice, the structural design of the railgun is controlled by requirements to both minimize the bore deformations and to provide the needed strength. Prevention of gap formation at the gun bore requires the structure to be preloaded so that the bore structural components are always maintained in compression. The desired 15 km/s projectile velocity in a 9.6 m long gun requires a rail current of at least 500 kA. Magnetostatic calculations [2] show that this current imposes a separating load of 2.6 MN/m on the rails. The maximum preload is controlled by the available bolting.

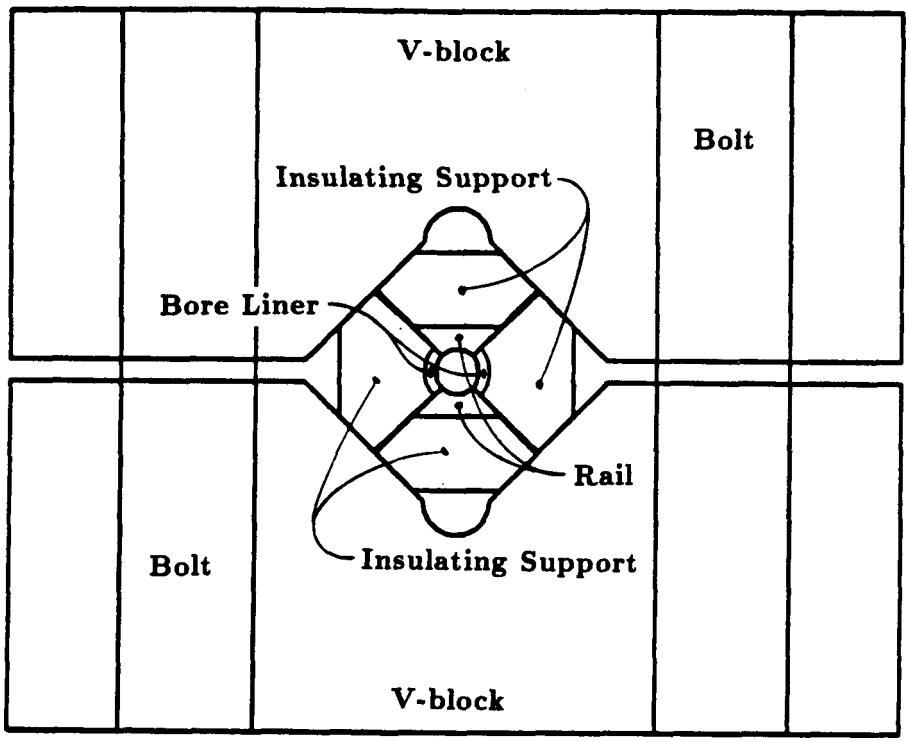

Figure 1.1. Cross-section Geometry of Railgun

This bolting allows a maximum preload of 18 MN/m (1,200,000 lb/ft). Increasing the preload, decreases the bore deformations under the operating loads while at the same time it increases the stress, strain, and the potential for failure of the bore components. This report documents the design process to achieve a gun bore structure which will maximize the allowable operating current.

Because of the expense and time required for fabrication of full scale components, structural analysis and model testing were performed to increase the probability of achieving a successful gun design. Analysis of the short test section railgun model was used to determine the deformations and stress states of the railgun components. Model testing was used to confirm the analysis, at specific sites where instrumentation was available, and to reveal behavior not well suited to analytical prediction. The knowledge gained from this model testing combined with the analysis of the model test was used to enhance the subsequent analysis of the actual, full-scale railgun structure.

2. Initial Gun Design

The railgun under consideration here is intended to be used in conjunction with a two-stage light gas gun. The gas gun will provide injection velocities into the railgun of 6 to 8 km/s. Therefore, the railgun bore must be compatible with the gas gun bore (i.e., a round bore is required). The initial gun design was selected based mainly on successful past practice [3]. The traditional bolted steel V-block was used to provide structural support to the gun bore components. An aluminum-oxide dispersion hardened copper, GLIDCOP-AL15, was selected for the rail material based on its electrical properties and strength at both room and high temperatures. A glass cloth reinforced epoxy, G-10 was selected for the primary insulating structural component which maintains the location of the rails within the V-blocks. The glass fibers of the G-10 make machining or other manufacturing operations difficult. Therefore, a polycarbonate bore-liner was placed at the gun bore between the rails and inboard of the G-10 so that the gun bore could be more readily honed to its final dimension.

2.1 Testing

2.1.1 Experimental Apparatus

A 160 mm section of the railgun was selected for testing. This section accurately represented the cross-section of the initial railgun design with the exception of the loading bolts. Because the structure was to be loaded in a servo-hydraulic test machine, the bolts were not required. Instead, the bolt loading was simulated by placing 38.1 mm (1-$\frac{1}{2}$ inch) wide steel plates between the test machine loading platens and the railgun V-block.

The railgun section was instrumented for the testing as follows:

1. Testing machine load cell
2. Clip-gage for rail bore displacement
3. LVDT for G-10 insulating support displacement
4. 3-LVDT's spaced along the V-block for V-block displacement and rotation
5. Strain gage rosette on rail bore

The instrumentation locations are shown in Figure 2.1.

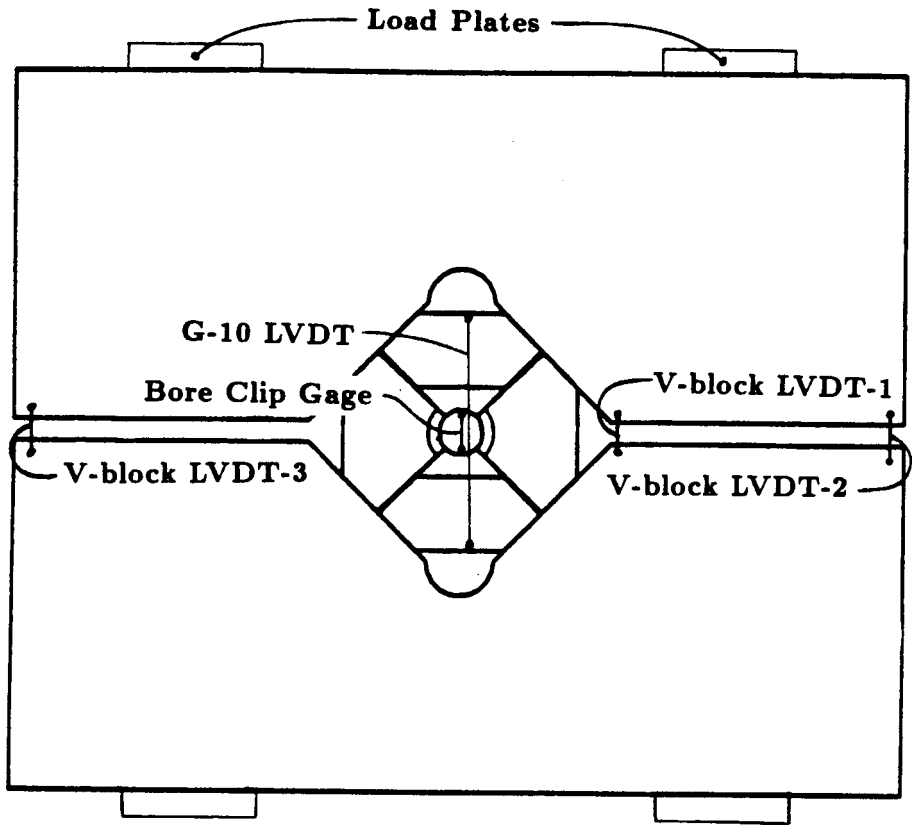

Figure 2.1. Instrumentation Location for Railgun Preload Test

2.1.2 First Test

Two tests of this railgun section were completed. In the first test, the load was applied as a steadily increasing ramp to 3 MN (700,000 pounds). This corresponds to a loading equivalent to 19 MN/m on the actual railgun. This is approximately the maximum load that can be applied to the railgun structure through the high strength bolts presently in use. At the maximum load, cracking of the G-10 insulator support blocks was noticed. Because this cracking was not expected, the load at which the cracking initiated was not determined. Subsequent review of the load versus displacement data indicated some anomalous behavior at a load between 1.33 MN and 1.78 MN. This behavior could be associated with G-10 cracking but cracking could not be confirmed as the cause. Another interesting phenomenon noticed at post test disassembly of the gun section was a layer of metal powder on the G-10 surfaces. This was due to a machining action of the glass fiber ends of the G-10 sliding along the surfaces of the steel V-block. This implies high friction at the contact between the G-10 and any other part. The load versus displacement data for the bore and the G-10

Table 2.1. Loading Sequence for the Second Railgun Core Segment Test

Increment	Load	Hold Time
1	0.46 MN (100,000 Lb)	1 min.
2	0.89 MN (200,000 Lb)	1 min.
3	1.33 MN (300,000 Lb)	1 min.
4	1.56 MN (350,000 Lb)	2 min.
5	1.78 MN (400,000 Lb)	2 min.
6	2.00 MN (450,000 Lb)	2 min.
7	2.11 MN (475,000 Lb)	2 min.

support are shown in Figure 2.2. The V-block displacements versus load are shown in Figure 2.3.

The G-10 insulating support displacement, Curve-2 in Figure 2.2, shows a reversal in the displacement between a load of 1.33 and 1.78 MN. This reversal is a possible indication of cracking (the only indication yet identified from this first test) in the G-10 supports. The V-block displacements are all very consistent with a greater displacement at the outer edges than near the bore. This is due to a slight amount of bending in the V-block. The results from the strain gages in the gun bore were quite erratic and not particularly useful in any case. Therefore, they are neither presented here nor were these gages used in subsequent tests.

2.1.3 Second Test

In the second test of the railgun section, 0.25 mm thick MYLAR was placed between the G-10 core and the steel V-Block. This MYLAR layer was introduced in the assembly of the actual railgun to provide an additional electrical insulating barrier between the rail and the V-block. It was included in this test to enhance the similarity between the actual railgun and the test section. The MYLAR sheet had the unanticipated structural effect of significantly reducing the friction between the G-10 supports and the V-block.

After the cracking of the G-10 experienced in the first test, the second test was performed in such a manner as to be able to determine the load at the onset of cracking more precisely. This was accomplished by applying the load in increments shown in Table 2.1.

A series of photographs was taken, one photograph at the end of each hold time

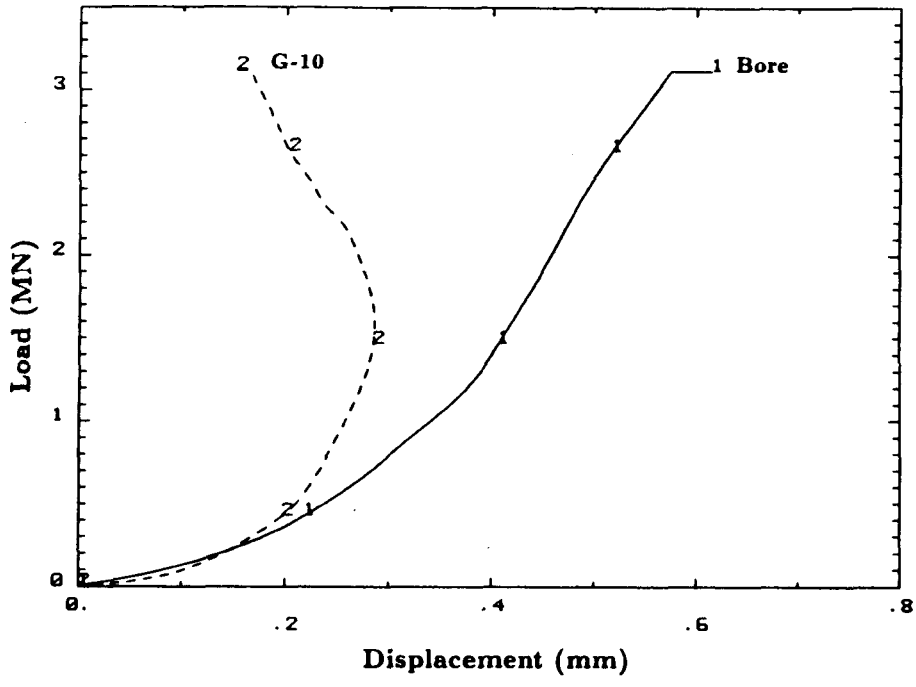

Figure 2.2. Bore and G-10 Displacements versus Load - Test 1

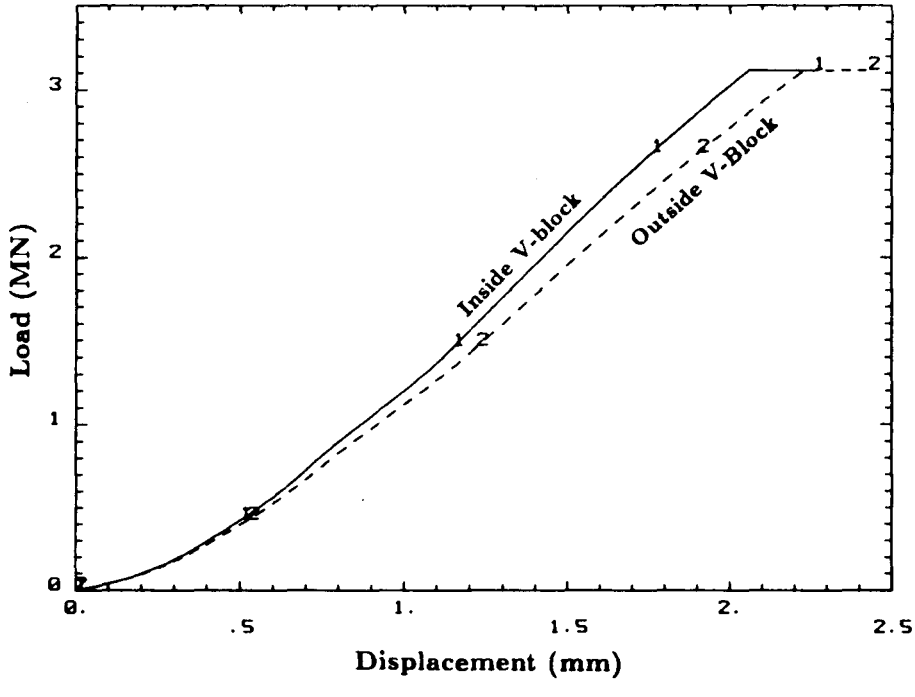

Figure 2.3. V-block Displacements versus Load - Test 1

along with several pre- and post-test photographs, in order to provide a permanent record. In addition, a close visual inspection of the structure was performed during the test to determine the onset of cracking in the G-10. The cracking was first observed at a load of 2.0 MN. The cracking was more readily seen at a load of 2.11 MN. In fact, cracks existed at a load of 2.11 MN at all 8 locations where the G-10 formed a corner with the V-Block resulting in a free surface. The test was stopped at a 2.11 MN load, and the test section was unloaded and disassembled, in order to check for internal cracking of the G-10 blocks. Internal cracking was roughly the same size as the corner cracks described above. The front face G-10 displacement versus load curve shows the same load reversal at 1.33 MN as observed in the first test. Because visual inspection did not reveal cracking at this level, this trend is a questionable indication of cracking. Thus, no reliable experimental evidence exists on the effects of the MYLAR layer on cracking of the G-10 insulating supports.

A series of load displacement data were taken with instrumentation similar to that described in the first test above. The bore and V-block displacements had the same trends but at slightly different levels than in the first test. In this second test, two displacement measurements of the G-10 insulating supports (shown in Figure 2.2) were taken, one on the front face and the other on the back face. Figure 2.4 shows the displacements versus load at the bore, the front face G-10, and the back face G-10. The V-block displacements versus load are shown in Figure 2.5.

In this test, because of the interrupted loading sequence, increasing (or decreasing) displacements were seen during the hold times in the loading. This is due to nonlinear behavior of unknown origin. It has been speculated that it may be caused by creep, cracking, or stick-slip friction. The visual inspection during and after the test make cracking an unlikely candidate mechanism, although cracking internal to the test specimen would not have been visible during the test. If stick-slip friction is responsible, its erratic nature makes further investigation unprofitable. Finally, in the actual railgun structure, the two V-blocks are bolted together. These bolts have been torqued and will be monitored for relaxation to determine if creep is the responsible mechanism.

The anomalous behavior of the displacement of the G-10 insulating supports in the first test and the difference between the front face and the back face G-10 displacements in the second test made comparisons between the computed and measured values of these parameters difficult. Therefore, the bore displacement and the V-block displacement provided the primary comparison between the analysis and the experiment. Because the V-block displacements were similar at all locations, only the inside (closest to the core structure) V-block displacement was used.

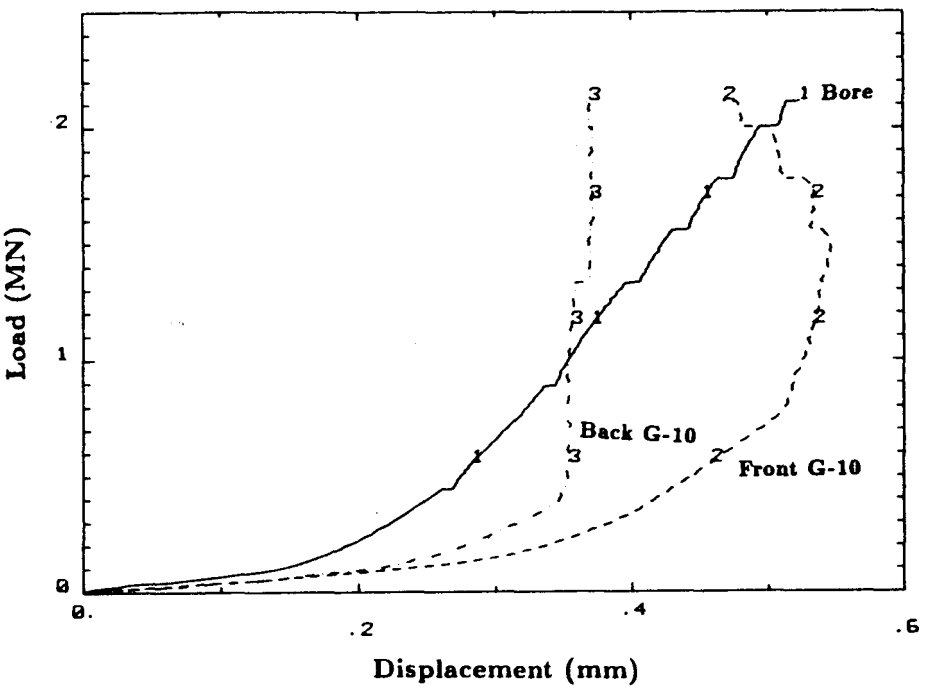

Figure 2.4. Bore and G-10 Displacements versus Load - Test 2

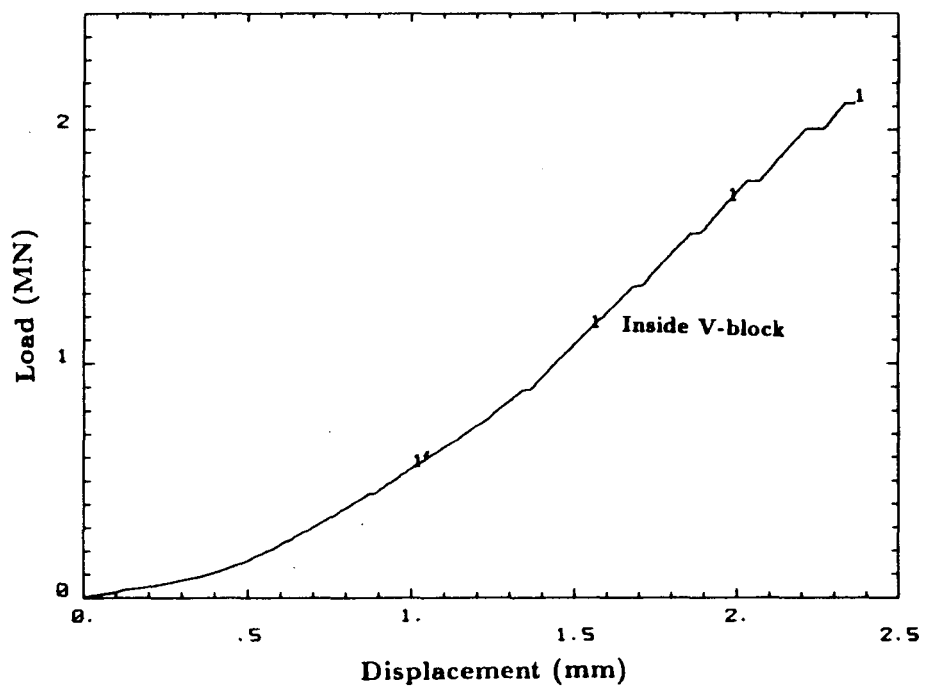

Figure 2.5. V-block Displacements versus Load - Test 2

2.2 Analysis

2.2.1 Finite Element Analysis Model

The railgun is a very complex structure to analyze. The structural response is highly nonlinear, primarily due to multiple intersecting contact surfaces with frictional effects. At high loads, plasticity also contributes to nonlinear behavior. While preloading the railgun is a quasi-static process, convergence of the static analysis codes was hindered by the intersecting and frictional contact surfaces. Therefore, the transient dynamic finite element analysis code, PRONTO-2D [4], was used to analyze the response of the gun to both the preload and the dynamic firing loads. PRONTO-2D has an extremely robust contact surface algorithm which had no difficulty with the railgun geometry. For preloading the gun, the load application in the PRONTO-2D calculations was slow enough that inertial effects were negligible. The railgun was assumed to be long enough to allow a plane-strain analysis while the short test section was assumed to behave in a plane-stress manner.

The finite element mesh for the structural analysis of the initial railgun design (shown in Fig. 2.6) was constructed using the preprocessing code FASTQ [5]. The same mesh was used for the analysis of the preload and dynamic firing loads. Because the preload problem was quasi-static, the use of the bolts in the analysis rather than loading plates of the model test, did not affect the results for the V-block or core structure. In the dynamic analysis of the firing loads however, the bolt stiffness was important. Thus, the use of the same mesh for these two purposes simply saves expense. Two axes of symmetry exist which permits modeling of only one fourth the structure.

There are three intersecting contact/sliding surfaces on the gun bore components. As required by the assumption of two-dimensionality, the bolt mesh overlays the mesh for the V-block. The bolt is attached to the V-block at the coincident nodes along the top of the structure. The loading plates in the scale model tests were located at this same position.

Five materials are included in this model, GLIDCOP AL-15 (an alumina dispersion hardened copper), Polycarbonate, G-10 (a glass cloth reinforced epoxy), steel V-block, and a high strength steel bolt material whose properties were modified to account for the differences in cross-sectional areas between the actual bolts and the two-dimensional approximation. All materials are modeled as isotropic elastic or elastic-plastic with a constant strain hardening slope. The material properties are shown in Table 2.2. Even though G-10 is anisotropic (literature values of E_1 range from 10 to 21 GPa and E_2 from 8 to 15 GPa with a variation in strength from 7 to 350 MPa) it was decided to analyze the G-10 as an isotropic material. The necessary constitutive theory for a nonlinear, anisotropic rate dependent material response is not currently available.

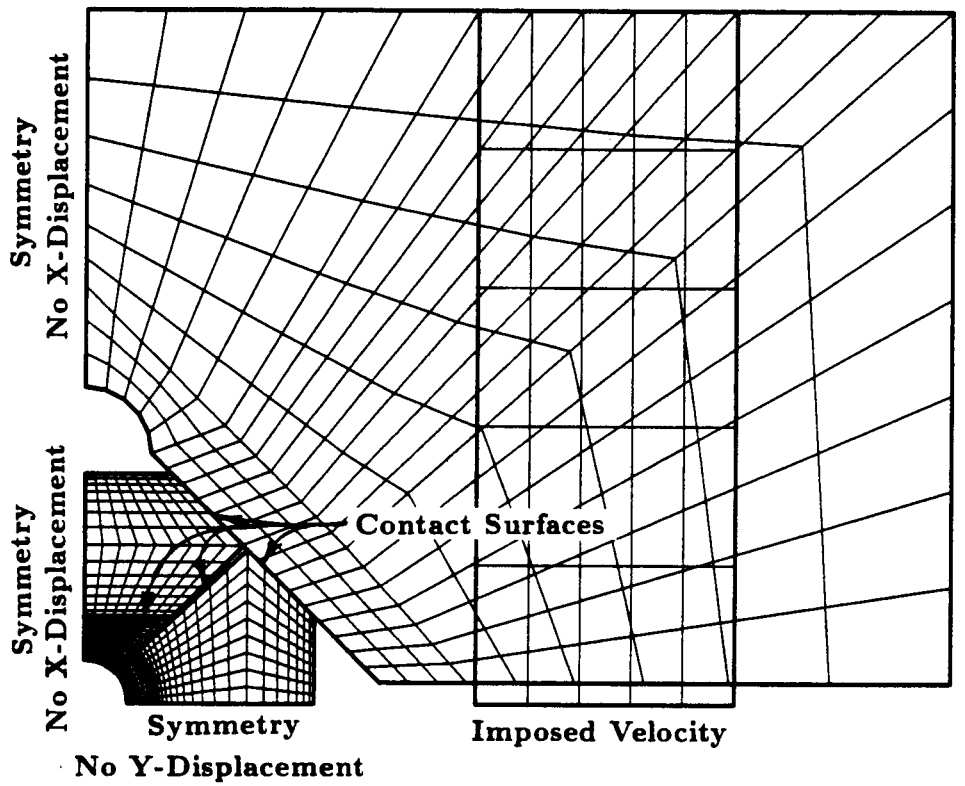

Figure 2.6. Finite Element Mesh of Railgun Cross-section

Development of such a theory will be pursued if it is shown to be required.

The PRONTO-2D code does not have a plane-stress formulation. For linear elasticity, if the material properties are altered as shown below, the use of a plane-strain formulation will result in a plane-stress solution [6]

$$E_{plane-stress} = E(1 - \nu^2) \tag{2.1}$$

$$\nu_{plane-stress} = \nu - \nu^2 \tag{2.2}$$

where E is Young's modulus and ν is Poisson's ratio. The mechanical properties of the materials used in the railgun are shown in Table 2.2. The elastic mechanical properties, altered to achieve a plane-stress solution, are shown in Table 2.3. The material properties for the isotropic idealization of G-10 shown in Tables 2.2 and 2.3 are a result of a series of analyzes with varying properties. The properties shown provided the best fit with the experimental data gathered from the short section testing.

The preload is a quasistatic process. Thus compression of the loading plates is identical to stretching the bolts as far as the transfer of load to the V-block and

Table 2.2. Mechanical Properties, Initial Design Railgun

Material	Density kg/m^3	Young's Modulus GPa	Poisson's Ratio	Yield Strength MPa	Hardening Modulus MPa
GLIDCOP AL-15	8.8×10^3	117.	0.37	400.	700.
Polycarbonate	1.2×10^3	2.38	0.4	59.	1.
G-10	1.8×10^3	12.0	0.4	*	*
Mild Steel	7.8×10^3	207.	0.3	310.	30.
Steel Bolt	2.1×10^3	55.4	0.3	*	*

* Elastic behavior

Table 2.3. Mechanical Properties, Initial Design Test; Adjusted for a Plane-Stress Analysis

Material	Density kg/m^3	Young's Modulus plane-stress equivalent GPa	Poisson's Ratio plane-stress equivalent	Yield Strength MPa	Hardening Modulus MPa
GLIDCOP AL-15	8.8×10^3	101.	0.233	*	*
Polycarbonate	1.2×10^3	2.00	0.24	*	*
G-10	1.8×10^3	10.1	0.24	*	*
Mild Steel	7.8×10^3	188.	0.21	*	*
Steel Bolt	2.1×10^3	50.4	0.21	*	*

* Elastic behavior

core structure is concerned. The non-linear dynamic analysis code PRONTO-2D was used for this solution primarily because of the robust nature of its contact surfaces. The loads were applied by imposing displacements on the bolt. Displacements were imposed slowly enough that inertia of the railgun components (in a global sense) was not important to the solution. The bolt displacement was applied by imposing a velocity boundary condition which ramped from zero to a maximum value of 0.5 m/s at 200 μs and then ramped back to zero at 400 μs resulting in a total displacement of 1.0 mm.

The railgun is fabricated with a nominal 1° angular gap between the G-10 supports of the railgun core. That is, when the gun components are in contact at the bore, a gap exists between the side and the top G-10 supports at the V-block under no load. This gap insures that the preload results in a hoop compression at the gun bore which is used to prevent a bore gap opening during firing loads. This gap also results in a rather complex stress distribution in the bore components. The ability to look at this distribution of stress at a load of interest identified by the experiment is one of the more beneficial results of a joint experimental and analytical program.

2.2.2 Analytical and Experimental Comparison

The analysis was compared with the experiment using the bore and the V-block displacements. The bore and V-block displacements versus load curves for the second test (with the MYLAR sheet) is compared to the curves from the frictionless analysis in Figure 2.7. A great variety of isotropic properties were tried in the attempt to idealize G-10 as an isotropic material. Young's Modulus was varied from the highest value found in the literature of 17 GPa to a low 5 GPa. Poisson's ratio was likewise varied from 0.49 to 0.05. Varying these parameters was required to determine the values applicable to the analysis of G-10 as an isotropic material under the specific loading conditions found in the railgun. The best fit to the experimental data shown in Figure 2.7 was found with the values shown in Tables 2.2 and 2.3 (Young's modulus of 12. GPa and Poisson's ratio of 0.4). These values correspond to a bulk modulus of 20 GPa and a shear modulus of 4.3 GPa. These values of bulk and shear modulus are near the top of the range found for plain, unreinforced epoxy. This indicates that the G-10 is loaded in the railgun in such a manner that the stiffening behavior of the glass fibers is not most effectively utilized.

The results of the first test, without the MYLAR sheet, are compared to the analysis using a coefficient of friction of 0.5 in Figure 2.8. In a manner similar to that used for selection of the most appropriate G-10 properties, a series of analyses was performed using coefficients of friction from 0.1 to 0.5. Very little difference in bore or V-block displacements were observed with coefficients of friction in this range.

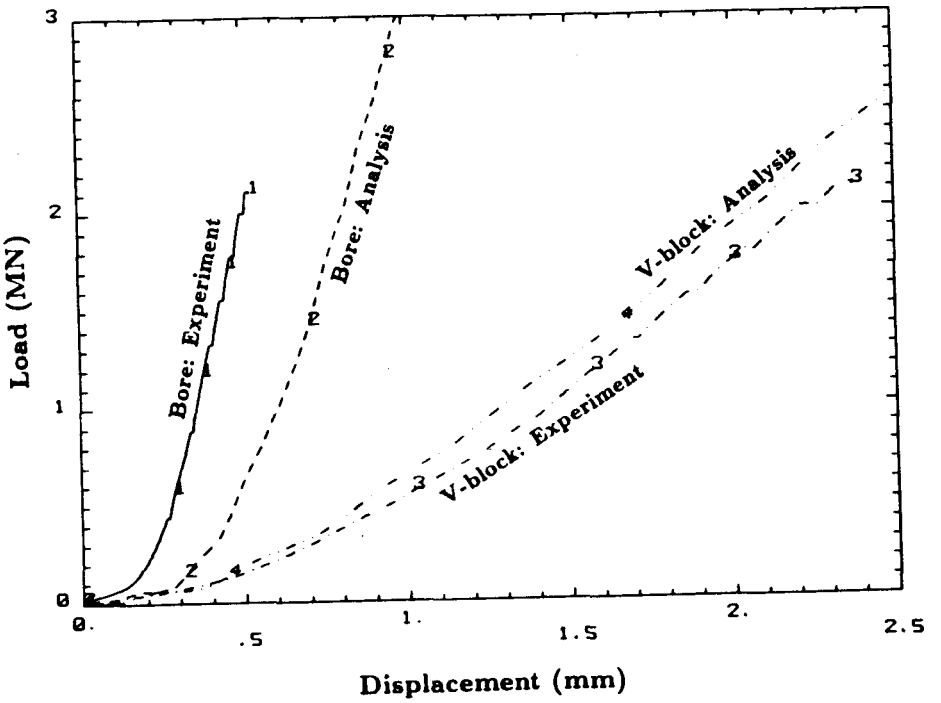

Figure 2.7. Comparison of Experiment and Analysis - Bore and V-block Displacements versus Load - No Friction

Therefore, a coefficient of friction of 0.5 was selected.

The load versus V-block displacements shown in Figures 2.7 and 2.8 indicate a very good agreement between the experiment and the analysis. This agreement was achieved through the process of varying the elastic parameters, Young's Modulus and Poisson's ratio. The agreement between the experimental and analytical bore displacements is worse. The same changes in elastic parameters had negligible effect on the bore displacements. The differences between the experimental and analytical load versus bore displacement can be divided into two parts. The first part can be regarded as a shift in the displacement at which the load starts to increase. This discrepancy is due to the difference in the starting point between the experiment and the analysis. Such a shift can result from manufacturing tolerances or initial positioning of the finite element mesh components and thus is of minimal concern. The second component is more important. There is a slight difference between the terminal slopes of the experimental and analytical load versus bore displacement curves. The analysis shows

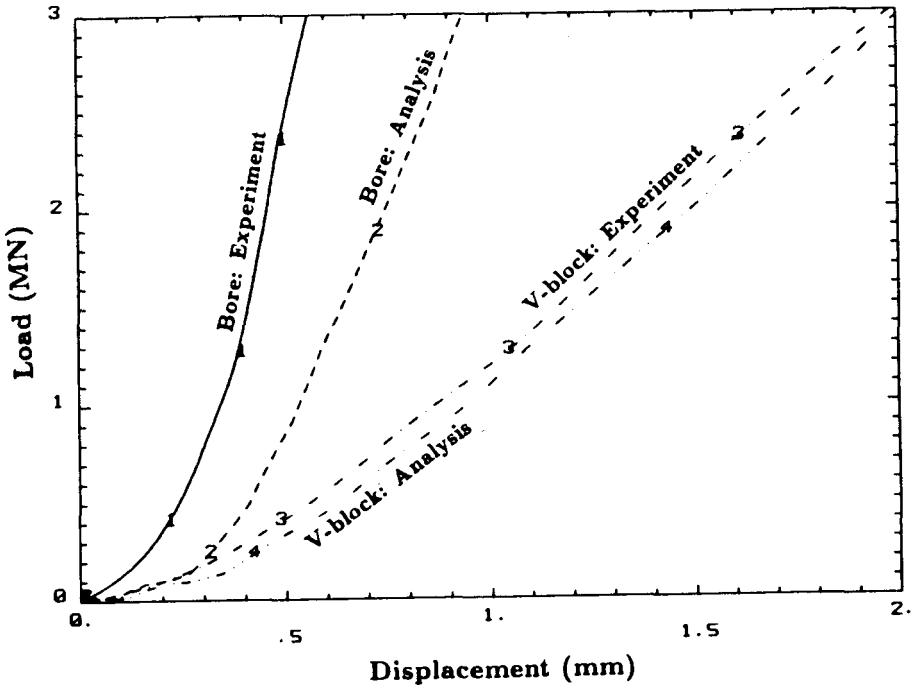

Figure 2.8. Comparison of Experiment and Analysis - Bore and V-block Displacements versus Load - with Friction

the softer behavior. Because changes in the elastic material properties had negligible effect on the analytical bore displacement, the bore displacements must be controlled by an as yet unidentified mechanism. These minor discrepancies in bore behavior were not considered critical to the goals of this program. The match between the experimental and analytical load - displacement curves shown above lends credibility to the analysis despite the concerns with accuracy of the material properties. It is felt that the analysis is adequate for its intended purpose, to make relative comparisons between various loads and boundary conditions.

2.2.3 Discussion of Results

Cracking occurred in the second test (with the MYLAR layer) at a load of approximately 2 MN. There are a great many criteria postulated for cracking in a fiber reinforced plastic. Only the two simplest potential criteria are investigated here. The

simplifying assumptions used in this analysis, discussed above, make the use of a more complicated criterion inappropriate. The two criteria are the postulation that cracking occurs when either the maximum shear stress or the maximum principal stress reach a critical value. The maximum shear stress results in a criterion often used for flow of ductile materials such as metals (plasticity). The maximum principal stress results in a criterion often used for brittle materials which break upon imposition of sufficient tensile stress.

The distribution of maximum shear stress at a load of 2 MN for the frictionless analysis (comparable to the test with the MYLAR layers) is shown in Figure 2.9. The distribution of maximum principal stress at the same loads is shown in Figure 2.10. In Figure 2.10 at the location of cracking, (in the corners of the G-10 support blocks) the maximum principal stress is negative or compressive. Thus the maximum principal stress criterion is not applicable because it is based on cracking due to tensile stresses not compressive stresses. Therefore, the maximum shear stress was selected as the more suitable criterion for the cracking of the G-10. From Figure 2.9, cracking of the G-10 can be anticipated at a maximum shear stress of approximately 250 MPa.

2.3 Application to Railgun Operation

Based on the cracking seen during the testing, it has been decided to reduce the preload on the actual railgun from the preliminary value of 0.775 MN (175,000 pounds) per bolt or 910 MPa (132,000 psi) bolt stress. A preload consistent with a 1.33 MN load on the test structure (approximately 8.4 MN/m (575,000 lb/ft; or 0.35 MN (75,000 lb) per bolt or 345 MPa (50,000 psi) bolt stress) will be applied. A plane-strain analysis was performed to simulate the response of the actual 2.4 m. long railgun. The MYLAR layer will be included in the assembly of the railgun to provide electrical insulation. Therefore, a frictionless contact between the V-block and the core components was employed. The maximum shear stress in the railgun cross section at 1.33 MN is shown in Figure 2.11. Comparison of the maximum shear stress at the location of cracking in the G-10 in Figure 2.11 (approximately 150 MPa) with the same location in Figure 2.9 (approximately 250 MPa) indicates a factor of safety of 1.6 is attained by reducing the preload.

Of course, this reduction in preload reduces the maximum permissible operating current in the railgun. In this case, the maximum operating current in the railgun is established based on the stress in the G-10, not on the formation of gaps at the gun bore. Loadings consistent with firing the gun at 300 kA and 400 kA were applied to the preloaded structure. These loads consisted of a plasma pressure on the inside diameter of the railgun for 10 μs followed by an effective magnetic pressure on the surfaces of the conducting materials (GLIDCOP rails and V-block) for a further 390

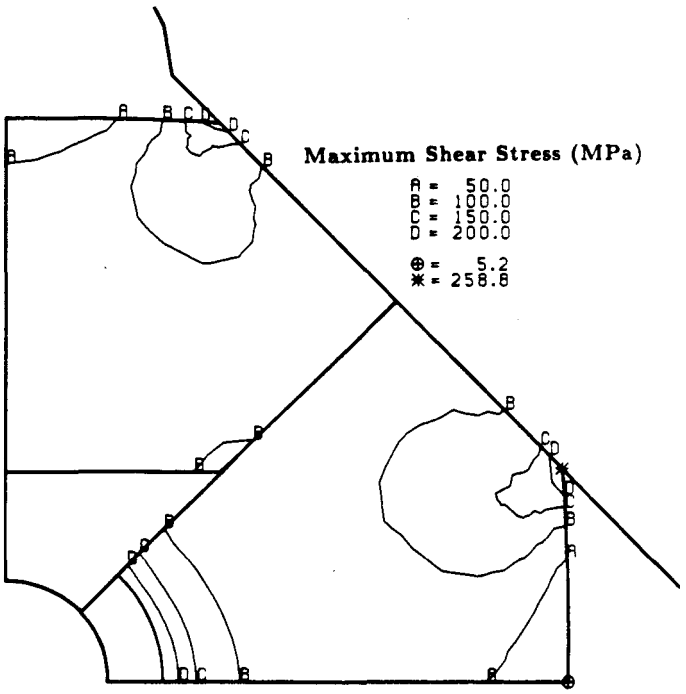

Figure 2.9. Plane-stress analysis of test section at a 2 MN Load; Maximum Shear Stress Contours

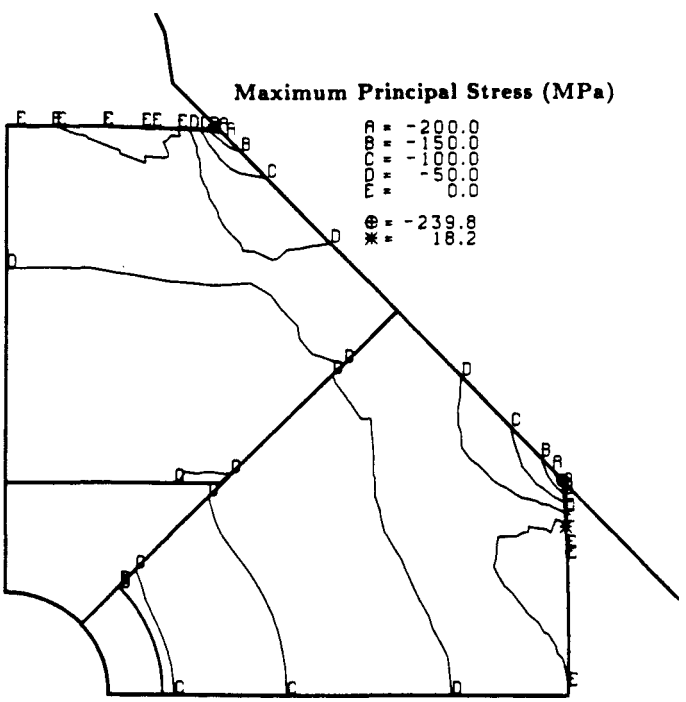

Figure 2.10. Plane-stress analysis of test section at a 2 MN Load; Maximum Principal Stress Contours

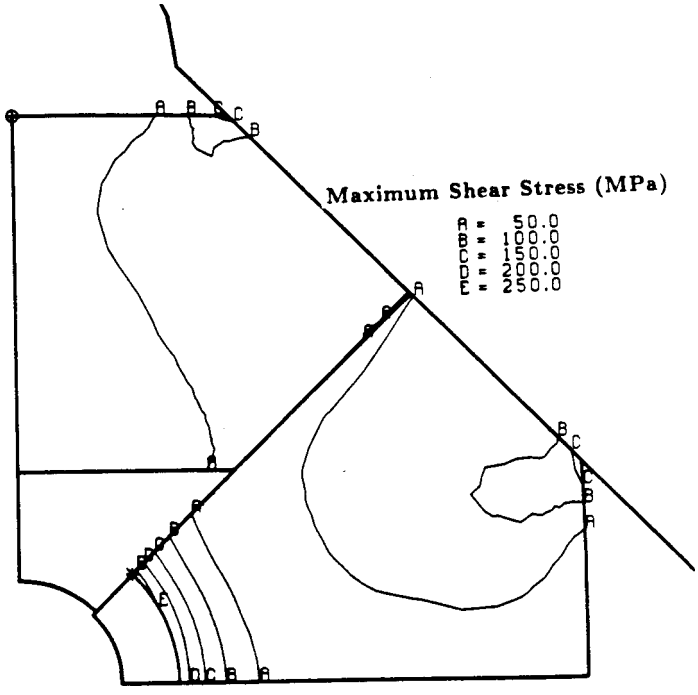

Figure 2.11. Plane-strain Analysis of Railgun at preload of 8.4 MN/m; Maximum Shear Stress Contours

μs [2]. The structural response was monitored for an additional 100 μs under no load. The analysis had a total duration of 500 μs. For both operating currents (300 kA and 400 kA) the maximum stress in the G-10 insulating support structure occurred on the rebound, after the operating loads had been removed. Maximum shear stress in the top G-10 support occurred at 410 μs (10 μs after load removal). For the side G-10 support, maximum shear stress occurred at 440 μs. The distribution of maximum shear stress in the gun core for an operating current of 300 kA are shown in Figure 2.12 at 410 μs and in Figure 2.13 at 440 μs. Figures 2.14 and 2.15 repeat the stress distributions at the same times for a 400 kA operating current. The maximum shear stress in the corners of the G-10 supports, where cracking occurred in the short section tests, reaches a peak value of approximately 200 MPa for 300 kA and 240 MPa for 400 kA. At 300 kA, the peak maximum shear stress in the G-10 does not increase significantly over that resulting from the preload. Operating currents up to 300 kA should not cause cracking of the G-10. At 400 kA, the peak stress in the G-10 reaches a value that resulted in cracking in the static model tests. Operating currents above 400 kA are likely to cause

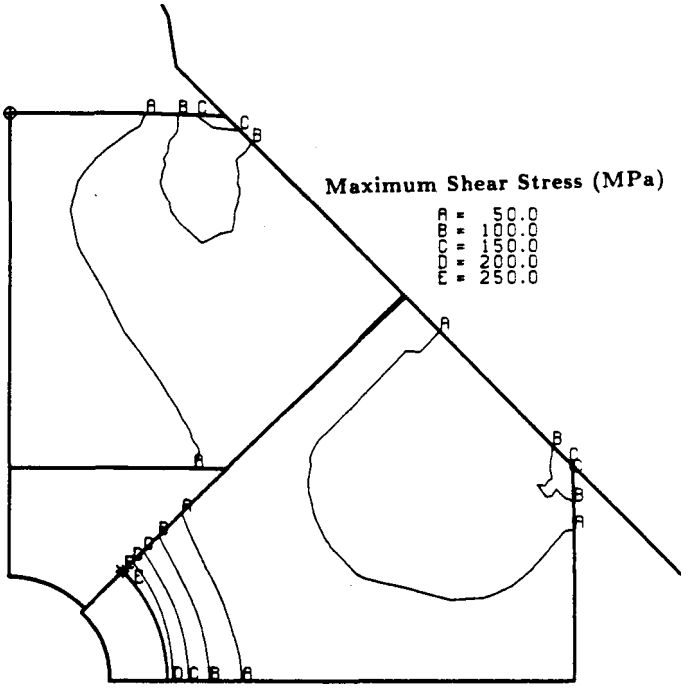

Figure 2.12. Maximum Shear Stress Contours at 410 μs at 300 kA Operating Current

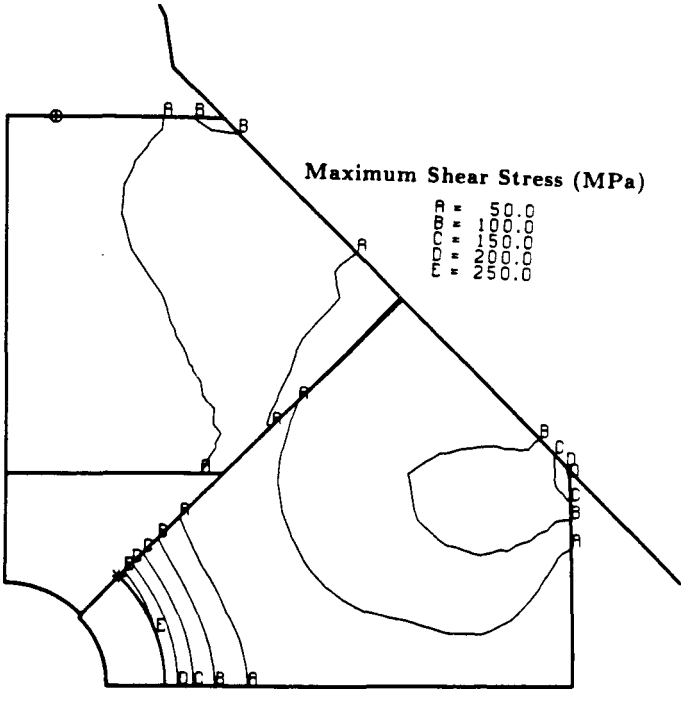

Figure 2.13. Maximum Shear Stress Contours at 440 μs at 300 kA Operating Current

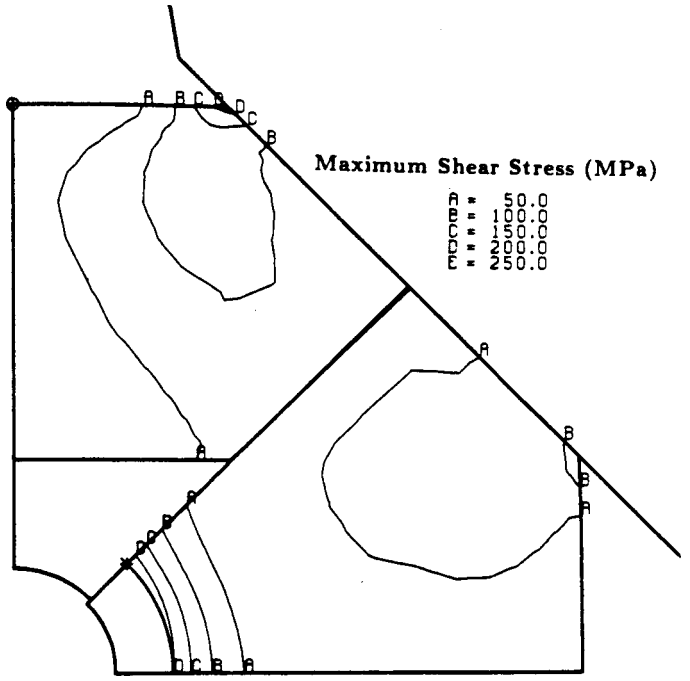

Figure 2.14. Maximum Shear Stress Contours at 410 μs at 400 kA Operating Current

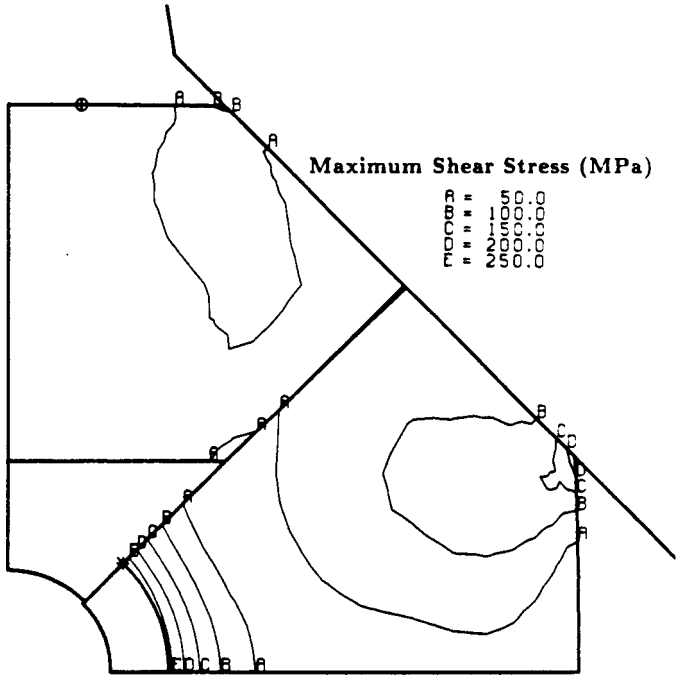

Figure 2.15. Maximum Shear Stress Contours at 440 μs at 400 kA Operating Current

cracking of the G-10. Between 300 and 400 kA, no definitive statement about cracking of the G-10 supports can be made. Conservatively, the operating current should be restricted to less than 300 kA for this initial railgun design.

3. First Design Modification - Trapezoidal Supports

The primary problem identified with the initial railgun design was the high shear stress and resulting potential for cracking in the corners of the G-10 insulating supports. This cracking potential limited both the allowable preload and the maximum operating current of the railgun. To reduce these shear stresses, steel trapezoidal supports were placed between the G-10 and the V-block as shown in Figure 3.1. These trapezoids eliminate the free surface on the back (outside) of the G-10 insulators. Thus the shear stresses imposed by this stress-free surface are minimized and the G-10 is subjected to a more uniform hydrostatic compressive stress state.

3.1 Testing

The 160 mm long railgun test section was again employed to verify this design modification. In addition to testing the steel trapezoidal supports, a polyimide bore liner was also tested as a replacement for the polycarbonate liner used in the testing of the initial design. The 0.25 mm thick MYLAR sheet material was again used between the G-10 core and the steel V-blocks. MYLAR was also applied between the segments of G-10 in the core. Therefore, all the contact surfaces were virtually frictionless. The same instrumentation as was used in the testing of the initial design, listed in section 2.1.1, was used for this testing with the exception of the rail bore strain gage rosette.

The test section was loaded in 22 kN (5000 lb) increments to 2.67 MN (600,000 lb), the maximum load capacity of the testing machine. The displacement gages were interrogated and the test piece was visually inspected for cracking every increment. The polyimide bore liner had a slightly smaller inside diameter than the polycarbonate liner used in the testing of the initial design. This reduced diameter caused the liner to interfere with the bore clip-gage early in the loading cycle. The clip-gage was unseated from its knife edges and the bore displacement measurement was lost. The inner V-block displacement (LVDT-1) versus load for the trapezoidal insert modified railgun design is shown in Figure 3.2. No cracking of the G-10 insulating supports or of the polyimide bore liner was observed. The maximum test load of 2.67 MN corresponds to a load on the actual railgun structure of 17 MN/m, very close to the maximum preload which can be applied with the present bolting scheme.

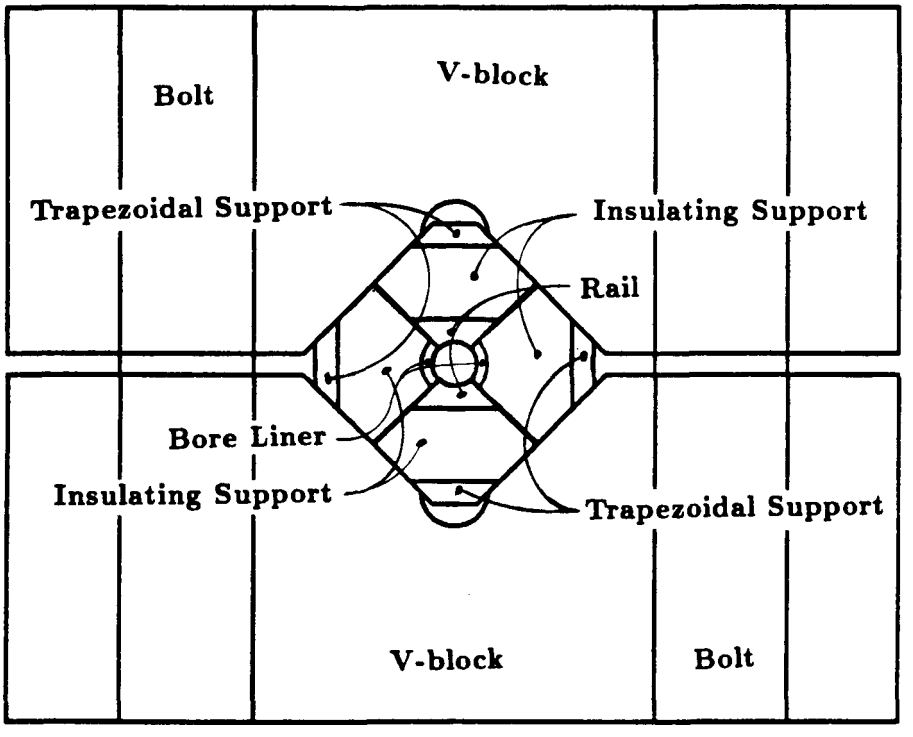

Figure 3.1. Cross-section of Railgun with Trapezoidal Supports

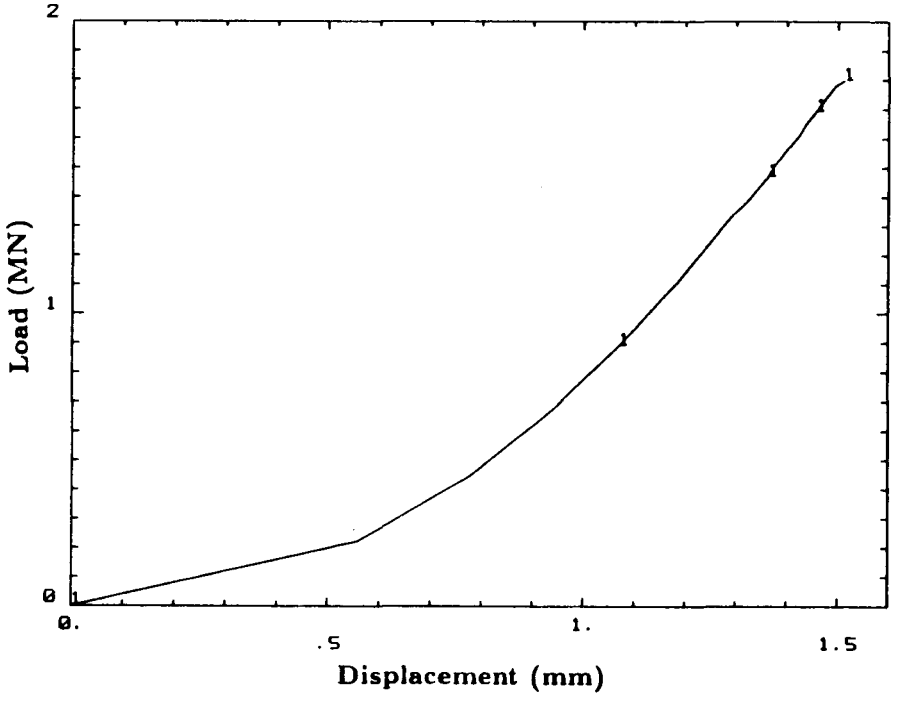

Figure 3.2. V-block Displacement versus Load - Trapezoidal Supports

3.2 Analysis

The finite element mesh used for the structural analysis of the railgun with the trapezoidal inserts is very similar to that explained earlier in detail in Section 2.2.1. The only difference in this mesh was the inclusion of the steel trapezoidal inserts. Consistent with the use of MYLAR sheet, all the interfaces were modeled as frictionless contact surfaces except for the bore liner which was glued to the G-10 support. The material properties used in the analysis of the test section were again adjusted to give a plane-stress solution as explained in Section 2.2.1. The actual (unadjusted) materials properties used are identical to those used in Chapter 2. The V-block displacement versus load results from the finite element analysis are compared to the experimental results in Figure 3.3. Analysis and experiment compare very well as was the case for the initial gun design described in Section 2.2.2.

The maximum shear stress in the G-10 is shown in Figure 3.4. Comparing this stress field with that shown in Figure 2.9 indicates the effectiveness of the steel trapezoids in reducing the shear stresses, particularly at the corners of the insulators where cracking was experienced in the initial railgun design. At the 2.67 MN load, the new design produces a peak maximum shear stress in the G-10 of approximately 125 MPa. This is half the value which caused cracking in the tests of the initial gun design (a factor of safety of 2).

3.3 Application to Railgun Operation

The loading of the actual 2.4 m long railgun module with steel trapezoidal supports was simulated by a plain-strain finite element analysis. The preload of 2.67 MN on the 160 mm long test section is equivalent to a load of 17 MN/m on the actual railgun structure. Analytically, the 17 MN/m preload was accomplished by displacing the end of the bolt 1.22 mm. For the plane-strain analysis, the maximum shear stress in the G-10 insulators again was approximately 125 MPa as shown in Figure 3.5. Compared to the value for the plane-stress analysis shown in Figure 3.4, the increased constraint of the plane-strain analysis had virtually no effect on the maximum shear stress.

The 17 MN/m preload using the trapezoidal supports was approximately twice the preload allowable with the initial railgun design described in Chapter 2. This increased preload permits the railgun to be operated at higher rail currents. The loading cycle for railgun operation, described in Section 2.3, was applied to this gun design for rail current magnitudes of 400 kA, 500 kA, and 600 kA. For both the 400 kA and 500 kA operating currents, no gap was formed at the gun bore. In both cases the maximum shear stress in the G-10 occurred 190 μs into the load cycle (90 μs after the magnetic pressure is applied to the rails). For 400 kA, the maximum shear stress in the G-10

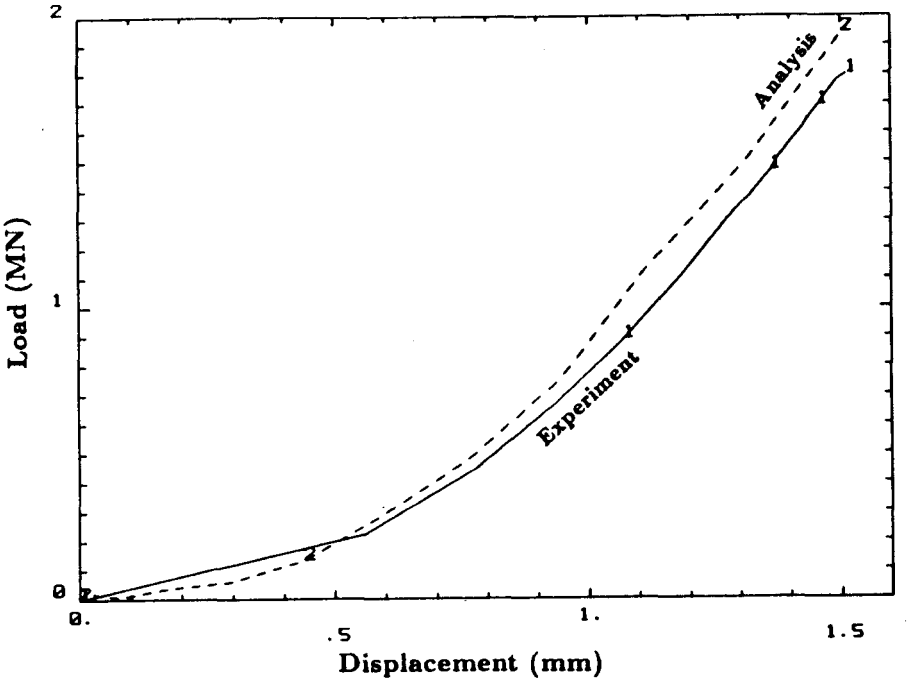

Figure 3.3. Comparison of Experiment and Analysis - V-block Displacement versus Load - Trapezoidal Supports

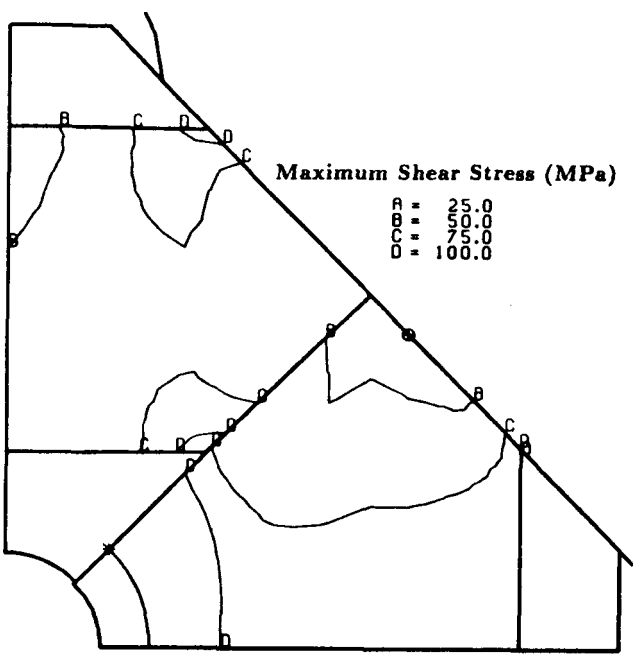

Figure 3.4. Plane-Stress Analysis of Test Section at 2.67 MN; Maximum Shear Stress Contours

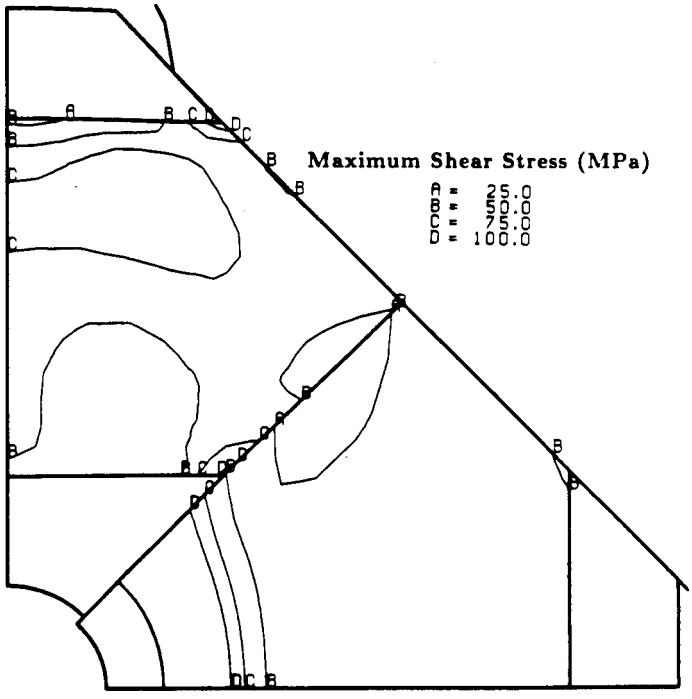

Figure 3.5. Plane-Strain Analysis of Railgun at a Make-up Load of 17 MN/m; Maximum Shear Stress Contours

was 180 MPa. The distribution of maximum shear stress at 400 kA is shown in Figure 3.6. This is well below the value shown to cause cracking of the G-10 in the testing of the initial gun design (Sections 2.1.2 and 2.1.3). For 500 kA, the maximum shear stress is slightly over 200 MPa (see Figure 3.7). Again this is less than the value shown to cause cracking. At a 600 kA operating current, a slight gap was formed at the gun bore. The maximum shear stress in the G-10 occurs 200 μs into the load cycle and reaches a peak magnitude of 240 MPa, shown in Figure 3.8. This is very close to the anticipated failure stress of 250 MPa. Operation of the railgun with the steel trapezoidal supports backing the G-10 insulators is acceptable up to 500 kA rail currents. At a rail current of 600 kA, both displacement and strength criteria are violated. Bore gaps are formed and the G-10 is likely to crack. Operating currents with this railgun design should be restricted to less than 600 kA.

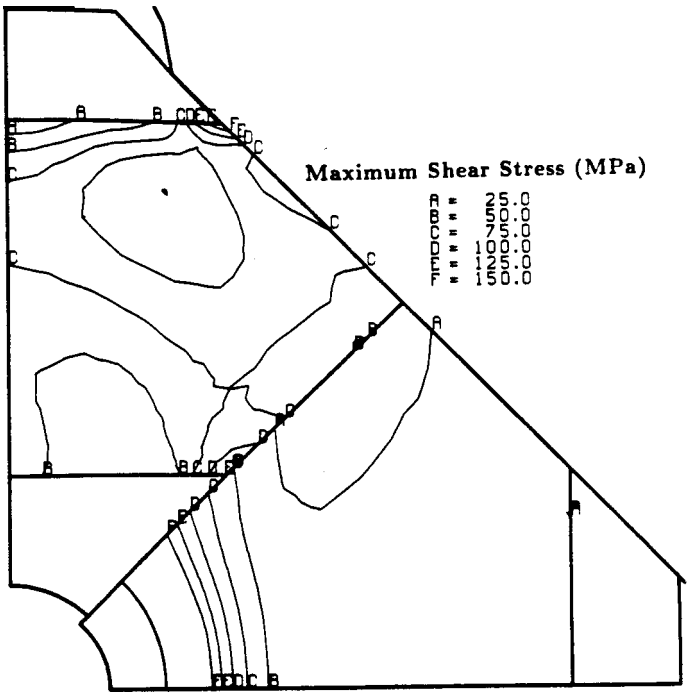

Figure 3.6. Maximum Shear Stress Contours at 190 μs for 400 kA Operating Current

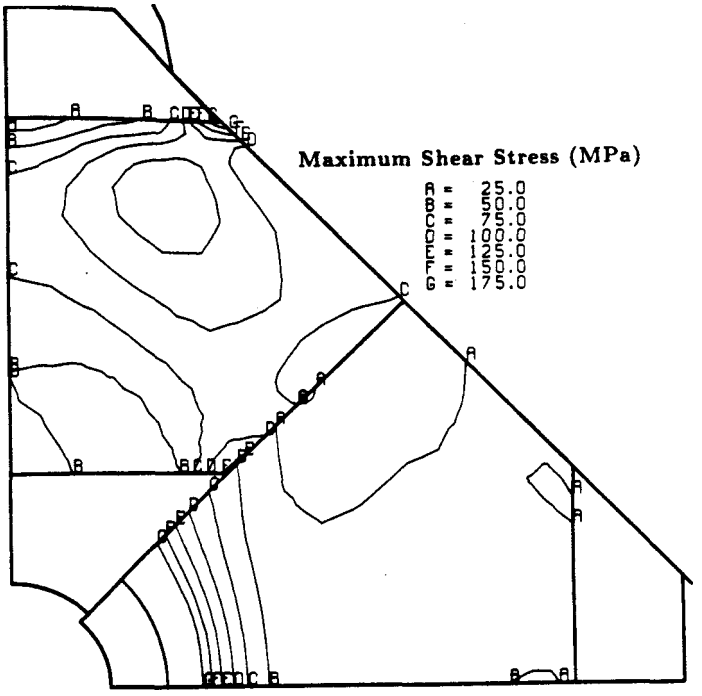

Figure 3.7. Maximum Shear Stress Contours at 190 μs for 500 kA Operating Current

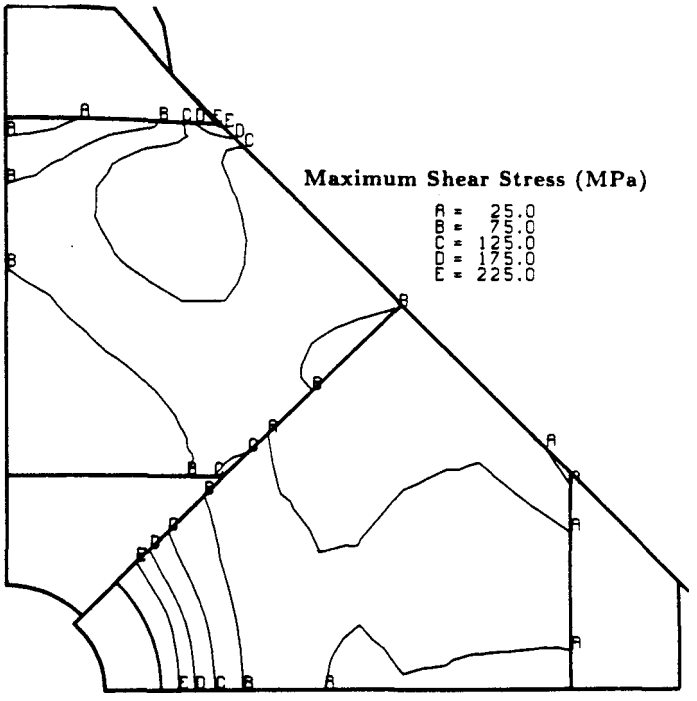

Figure 3.8. Maximum Shear Stress Contours at 200 μs for 600 kA Operating Current

4. Second Design Modification - Ceramic Insulators

The high shear stress and resulting potential for cracking of the G-10 insulating supports was reduced but not eliminated by the use of the steel trapezoidal supports described in Chapter 3. Even with the use of the trapezoids, the operating current in the gun rails is limited to less than 600 kA. For higher operating currents, a higher preload is needed which requires the strength of the insulating support material to be increased. The use of alumina (Al_2O_3) ceramic insulating supports to replace the G-10 supports was the next design investigated. Because the stress state in the gun core components is dominated by a hydrostatic compressive field, it was anticipated that a high strength, though brittle, material such as alumina would withstand the shear stresses better than the G-10 composite. To achieve the benefits of an increased preload allowed by the higher strength ceramic supports, the strength of V-block material must also be increased and a new means developed to apply the higher preload.

4.1 Testing

A series of four tests on varying lengths of ceramic supports was performed. All four tests were performed with the same 160 mm long V-block test section used in the prior testing. The plastic (polycarbonate or polyimide) bore liners were not included in the testing because they interfered with the bore clip gage and their contribution to the structural response of the test section was negligible. MYLAR sheet material was used between the ceramic and the steel V-blocks and between the ceramic and the Glidcop rails. When assembled, it was necessary to apply multiple MYLAR sheets to the surfaces where the ceramic would contact ceramic in the gun core in order to eliminate gaps. These gaps were caused by the rail segments used in the test being slightly oversized and by the use of a thicker than anticipated MYLAR layer between the rail and the ceramic support. The use of MYLAR resulted in virtually frictionless contact surfaces. The instrumentation and hydraulic testing machine was the same as used for the testing described in Chapter 3. As was the case in Chapter 3, positive displacement indicates a closing motion or a decrease in separation of components.

In the first test, the ceramic support pieces were the full 160 mm length of the V-block test section. The test section was compressed in the hydraulic test machine in 44.5kN. (10,000 lb.) increments to the full 2.67 MN. (600,000 lb.) capacity of the hydraulic test machine. The bore displacement and V-block displacement versus load curves are shown in Figure 4.1. Both the bore and the V-block displacements are nearly linear with load above 50 kN. The initial nonlinearity is attributed to initial "seating"

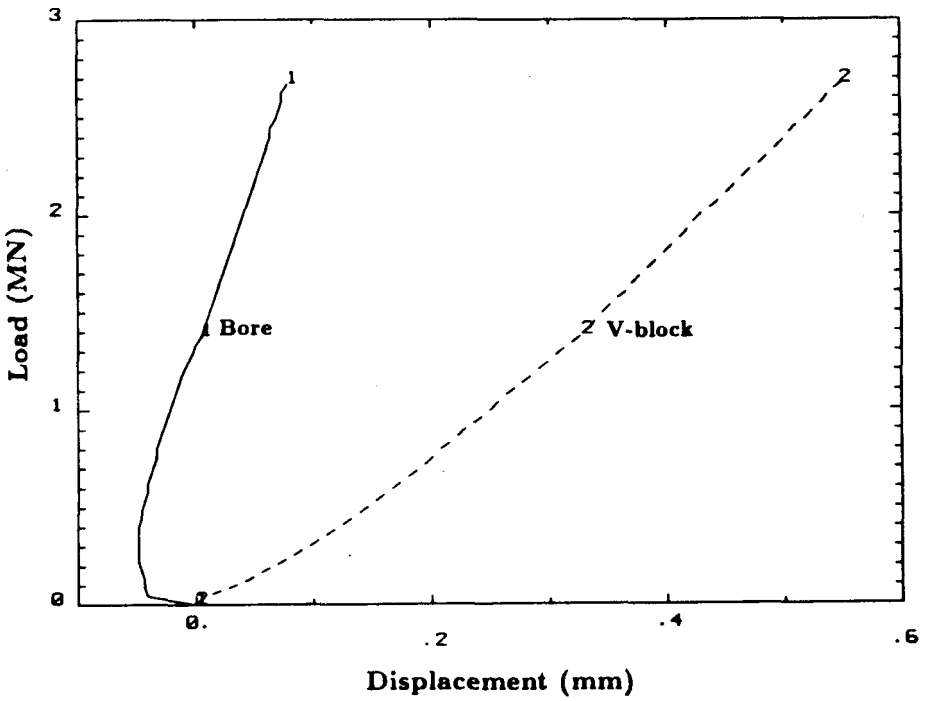

Figure 4.1. Bore and V-block Displacement versus Load - Full Length Ceramic Core

displacements and to the behavior of the compliant MYLAR layers. No evidence of any cracking of the ceramic was seen either during the test or upon posttest disassembly and inspection. There was a slight mark on the GLIDCOP rail where the side ceramic piece was in contact, indicating some plastic deformation of the rail by the ceramic. There was no evidence of any distress on the V-block.

This first test demonstrated the ability of the ceramic supports to withstand a compression of 2.67 MN over the full length of the test section which is equivalent to 17 MN/m. This is the same load borne by the G-10 supports with the trapezoidal steel backing. The ceramic supports must have a higher capacity than the G-10 supports in order to be worthwhile. For application to the railgun design, it is not the absolute load carried in the test section but the load per unit length that is of most importance. Because the test machine load limit had been reached in the first test, it was decided to reduce the length of the ceramic test pieces. The 160 mm long ceramic supports were cut into 51 mm long sections.

For the second test, two of the 51 mm long ceramic support pieces were used to

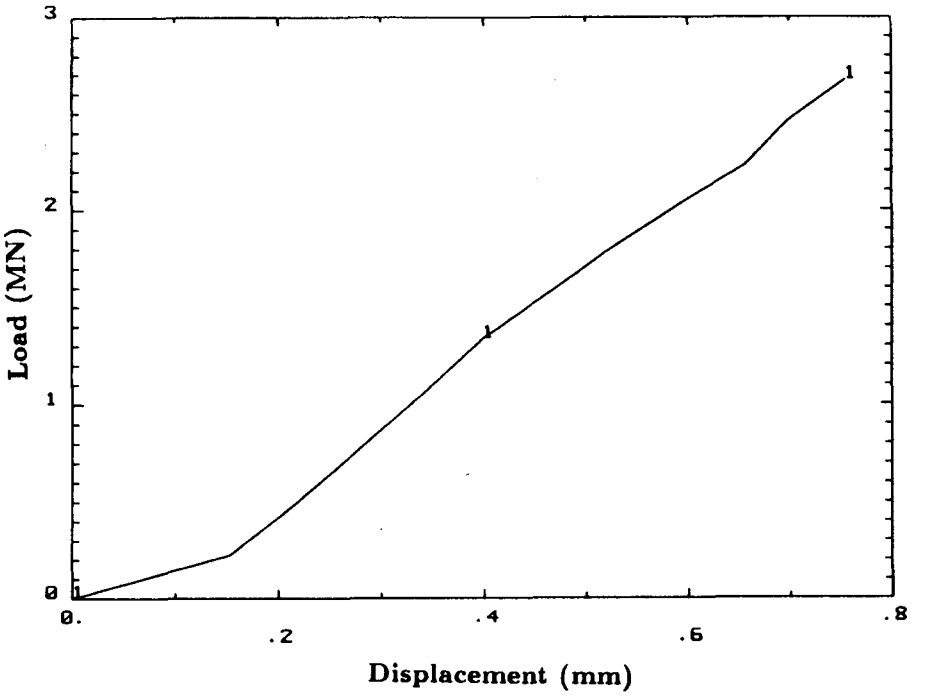

Figure 4.2. V-block Displacement versus Load - 102 mm Long Ceramic Core

give a test length of 102 mm. The full 160 mm V-block section was used with the ceramic pieces positioned at the ends of the V-block to minimize cocking or bending of the test section. This arrangement resulted in a nominal 60 mm gap (without core sections) at the center of the V-block. There was a greater concern for the potential catastrophic failure of the ceramic supports in this test than in the first test described above. Therefore, the bore displacement clip gage was not included in this test. For this test, the load was applied in 220 kN (50,000 lb) increments until the 2.67 MN capacity of the test machine was reached. The V-block displacement versus load is shown in Figure 4.2. For the total 102 mm length of ceramic tested, 2.67 MN results in a 26 MN/m load per unit length which is 1.5 times that of the first test. As in the first test, no evidence of cracking of the ceramic supports could be found either during the testing or upon disassembly and inspection. The rails were plastically deformed by the ceramic with a faint but perceptible step remaining where the ceramic side support contact ended. Again, there was no evidence of plastic deformation of the V-block.

The third test was similar to the second test except that only one of the 51 mm long ceramic core sections was employed. This 51 mm ceramic core was placed at

the axial center of the 160 mm long V-block section. As in the second test, the bore displacement clip gage was not employed. The load was applied in 220 kN increments to the 2.67 MN test machine capacity. The load versus V-block displacement curve is shown in Figure 4.3. Starting at approximately 1.5 MN (400,000 lb.), noises indicating possible cracking of the ceramic cores were heard throughout the remainder of the test. Upon disassembly of the test section, the ceramic core pieces were found to be cracked perpendicular to the gun axis. There was no evidence of cracking on any other plane. The rails were deformed in the same pattern seen in the prior two tests but to a greater extent. The step formed by the end of the ceramic side support was approximately 3 mm deep. In addition, the V-blocks had an indentation approximately 1.6 mm deep corresponding to the location of the ceramic support pieces. The curvature of the load versus displacement curve of Figure 4.3 is attributed primarily to the plastic deformation of the V-block with the axial cracking of the ceramic playing an insignificant role.

The cracking of the ceramic can be explained by the nature of the test setup. Because the V-block was longer than the ceramic core section, axial bending moments were introduced in the test. The local plastic deformation of the V-block tended to increase the axial bending applied to the ceramic. This explanation of the cracking is confirmed by one crack in the topmost piece of ceramic. This crack initiated at the uppermost edge (extreme fiber where the tensile stress due to bending was a maximum) of the ceramic piece but did not propagate entirely through the cross-section. At the inside edge, this ceramic piece was still unbroken. For the actual railgun structure, the V-block and the ceramic core will be the same length and will be uniformly loaded along their length. Therefore, the axial bending introduced in this test will not occur in the actual railgun. Because no cracking on any other plane was experienced, the ceramic supports in the actual railgun structure should withstand a preload of at least 51 MN/m, consistent with the loading of 2.67 MN applied over the 51 mm length of this test.

The fourth test was simply a repeat of the third test with the inclusion of the steel trapezoids used to back up the G-10 in the earlier design modification. The load versus V-block displacement curve is shown in Figure 4.4. The increased displacements seen in Figure 4.4 over those of Figure 4.3 were due to the presence of the local plastic indentations in the V-block remaining from the prior test. The noises indicating the initiation of cracking in the ceramic core pieces commenced at about the same load level as in the third test and the post test inspection revealed the same pattern of cracks perpendicular to the gun axis. The rail and V-block deformations were virtually identical to those of the previous test. The steel trapezoids had no apparent effect on the behavior of the ceramic railgun core structure. Their use or omission should be based solely on assembly considerations.

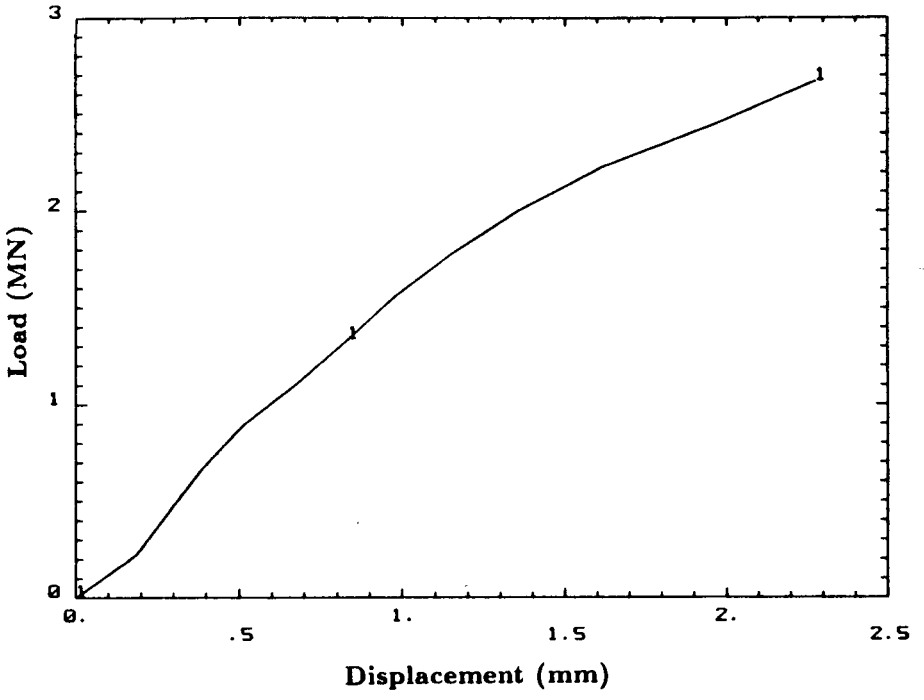

Figure 4.3. V-block Displacement versus Load - 51 mm Long Ceramic Core

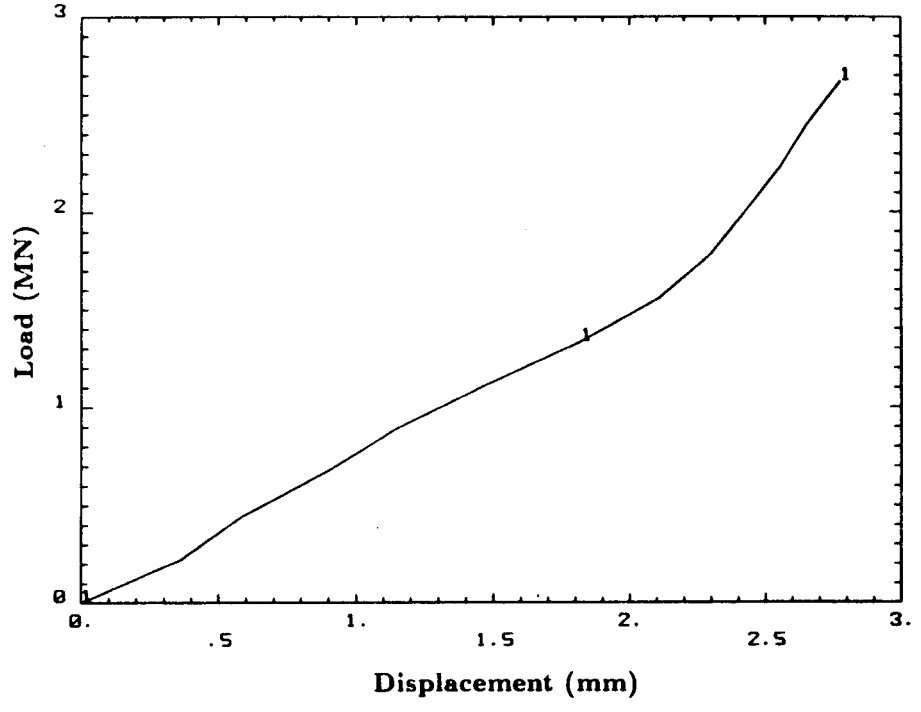

Figure 4.4. V-block Displacement versus Load - 51 mm Long Ceramic Core with Trapezoidal Supports

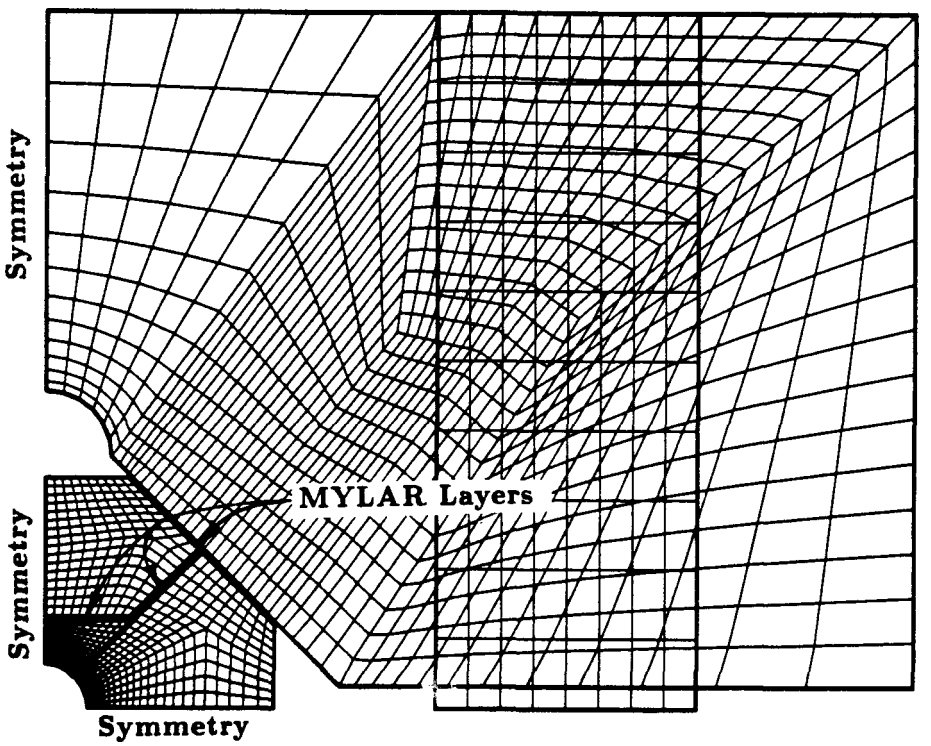

Figure 4.5. Finite Element Mesh for Analysis of Ceramic Core Tests

4.2 Analysis

The finite element mesh used for the structural analysis of the ceramic cored railgun is shown in Figure 4.5. This mesh is similar to the meshes used earlier in Chapters 2 and 3. As in the prior analyses, all contact surfaces were assumed to be frictionless and the elastic properties of the materials were adjusted to obtain a plane-stress solution. These adjusted mechanical properties used in the analysis of the ceramic core tests are shown in Table 4.1. Due to the increased stiffness of the ceramic core structure, it was necessary to include the compliant MYLAR layer in the analysis in order to match the experimental load versus displacement results. Because the yield strength of the MYLAR is low in comparison to the other core structure materials and because high loads were applied, the MYLAR's elastic behavior was relatively unimportant to the overall structural behavior of the railgun section test. The effect of the MYLAR on the test section response was primarily controlled by the post yield behavior and the thickness of the MYLAR layers. From the gun section testing, it was not possible to separate these results. Therefore, the mechanical properties of

Table 4.1. Mechanical Properties Ceramic Core Test; Adjusted for a Plane-Stress Analysis

Material	Density kg/m^3	Young's Modulus GPa	Poisson's Ratio	Yield Strength MPa	Hardening Modulus MPa
GLIDCOP AL-15	8.8×10^3	101.	0.23	231.	404.
Alumina	3.8×10^3	282.	0.18	*	*
Mild Steel	7.8×10^3	188.	0.21	*	*
Steel Bolt	2.1×10^3	50.4	0.21	*	*
MYLAR	1.4×10^3	3.	0.24	70.	100.

* Elastic behavior

the MYLAR were assumed to be the handbook values shown in Table 4.1 and the thicknesses of the various layers were adjusted in a series of analyses. The analytical bore and V-block displacement versus load curves compared to the experimental results from the first test (full test section length ceramic core) in Figure 4.6 are the results from this series of analyses which best fit the experiment. In this case 0.66 mm of MYLAR were used between the GLIDCOP rail and the ceramic, 0.54 mm between the V-block and the ceramic, and 0.85 mm in the space where the ceramic would meet ceramic. The rational behind changing the MYLAR thicknesses was based on the manner in which the test section was assembled. The short core pieces were placed in the V-blocks and obvious gaps were filled with MYLAR sheet material. It was possible that this procedure resulted in unseen gaps between the thin MYLAR layers. Thus, the effective thickness of the MYLAR could differ from the thickness of the number of sheets used at any given location.

For brittle materials such as ceramics, the maximum normal stress theory of failure is appropriate. That is, failure may be anticipated when the maximum normal (principal) stress reaches a critical value. For alumina, the critical stress in tension is approximately 275 MPa (40,000 psi). At the maximum load applied in the first test, 2.67 MN, the peak value of maximum principal stress in the ceramic core was less than 100 MPa (see Figure 4.7). Most of the stresses in the core were compressive with only small local regions of tensile stress. The lack of any high tensile stresses in the ceramic core materials is consistent with the experimental results in which no cracking was observed.

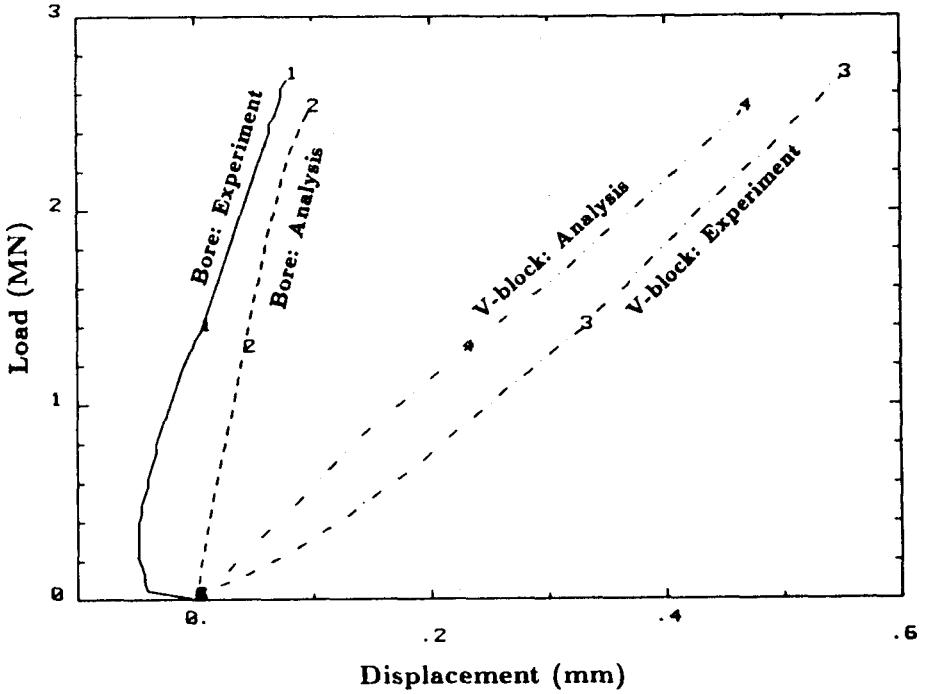

Figure 4.6. Comparison of Experiment and Analysis - Bore and V-block Displacements versus Load - Full Test Section Length Ceramic Core

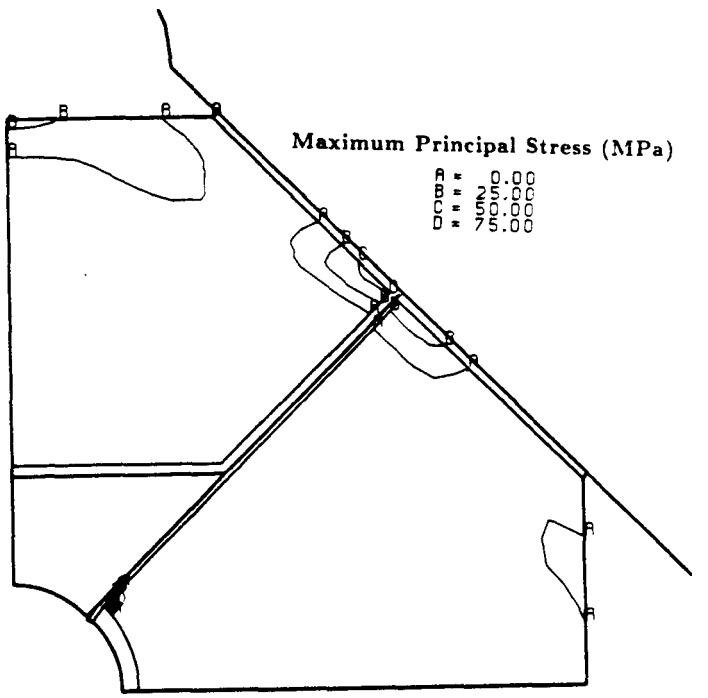

Figure 4.7. Distribution of Maximum Principal Stress in the Full Length Ceramic Core Railgun Test Section at 2.67 MN

Table 4.2. Mechanical Properties Ceramic Core Railgun; High Strength V-block and High Stiffness Bolt

Material	Density kg/m^3	Young's Modulus GPa	Poisson's Ratio	Yield Strength MPa	Hardening Modulus MPa
GLIDCOP AL-15	8.8×10^3	117.	0.37	400.	700.
Polycarbonate	1.2×10^3	2.38	0.4	59.	1.
Alumina	3.8×10^3	310.0	0.24	*	*
Q and T Steel	7.8×10^3	207.	0.3	830.	10.
Modified Bolt	2.1×10^3	166.	0.3	*	*
MYLAR	1.4×10^3	3.0	0.24	70.	100.

* Elastic behavior

4.3 Application to Railgun Operation

As explained earlier and demonstrated by the testing, in order to make use of the increased strength and stiffness of the ceramic core supports, an increase in V-block strength as well as an increase in preload capacity must be provided. The material properties of the V-block were changed from those of a mild steel with a yield of 310 MPa to those of a quenched and tempered steel with a yield of 830 MPa. The increased capacity preload scheme has not yet been designed, but it will require a greater effective cross-section area than is available with the bolts presently used. For the purpose of this investigation, a simple increase in the stiffness (Young's Modulus increased by a factor of 3) of the present bolt model was used. These changes in mechanical properties used in the analysis are shown in Table 4.2. Because the actual railgun is 2.4 meters long, its behavior was adequately represented by plane-strain assumptions. The ceramic core supports, rails, and V-blocks for the actual railgun will be precisely fabricated and assembled. Therefore, the nominal 0.36 mm MYLAR sheet thickness was used at all contacting surfaces rather than the variable thicknesses used in the preceding analysis of the test section.

In this analysis, the railgun cross-section was loaded by imposing a 0.31 mm displacement of the bottom of the bolt resulting in a 35 MN/m preload. At a 35 MN/m preload, the maximum von Mises equivalent stress in the V-block is 575 MPa. For a quenched and tempered steel at a yield strength of 830 MPa, a 575 MPa stress results in a factor of safety 1.4. The maximum von Mises equivalent stress in the rail is 397 MPa (see Figure 4.8), very close to the yield strength (400 MPa.) of the GLIDCOP rail material. A rail stress just short of yielding is the ideal stress state to prevent gap formation under operating loads. Therefore, 35 MN/m (twice the preload

that can be used with the G-10 insulating supports) appears to be the optimum value. At the 35 MN/m preload, the maximum principal stress (tension) in the ceramic core structure is 117 MPa, shown in Figure 4.9. Comparing the 117 MPa tensile stress with the nominal tensile strength of Alumina ceramic, 275 MPa, indicates that there should be no cracking of the ceramic supports under the preload. The location of this tensile stress, confined to a very local region near the intersection of the side ceramic support, the GLIDCOP rail, and the polycarbonate bore liner, reduces the potential for harmful cracking even further.

The increased preload along with the increased stiffness of the core and bolting resulting from the use of an Alumina core support structure permits the railgun to be operated at higher rail currents. The loading cycles for railgun operation, described in Section 2.3, with loading magnitudes consistent with rail currents of 600 kA, 700 kA, and 800 kA were analysed.

At a 600 kA rail current, a small 10 μm gap is formed at the gun bore. This gap is due primarily to the inability of the low strength polycarbonate bore liner to accept a high preload. Between the rail and the ceramic side support behind the bore liner, no gap is formed. The small gap limited to the dimension between the rail and bore liner is unlikely to be harmful to the gun operation. The maximum von Mises equivalent stress in the rail occurs 440 μs into the load cycle. This is during the rebound of the core components after the operating loads have been removed. There is a small amount of yielding that occurs in the corner of the rail where the rail contacts both the top and side ceramic supports, shown in Figure 4.10. The volume of yielded material is quite small and is contained within an elastic region. No detrimental effects are expected. The peak value of maximum principal stress in the ceramic also occurs on rebound from the operating loads, at 460 μs into the load cycle shown in Figure 4.11. This largest principal stress is 137 MPa at the same location as the peak stress caused by the preload. This stress is much less than the 275 MPa tensile strength of the alumina.

At a rail current of 700 kA, a 70 μm gap forms at the bore with a 20 μ gap between the rail and the ceramic. At 130 μs into the loading cycle (while current is still flowing), the peak von Mises equivalent stress is reached in the rail. The primary yielding of the rail is at the same location as described above for the 600 kA load. However, there is also a very local yielding at the centerline of the rail bore shown in Figure 4.12. The maximum principal stress in the ceramic also occurs 130 μs into the loading cycle. The peak value, shown in Figure 4.13, is 150 MPa which is well below the tensile strength of the ceramic. The formation of gaps at the gun bore, as well as yielding of the rail at the bore, indicate that operation of the gun at 700 kA is marginal at best.

At 800 kA, the gun behavior is clearly unacceptable. Large gaps (0.15 mm at the bore and 0.06 mm between the rail and the side ceramic support) are formed over

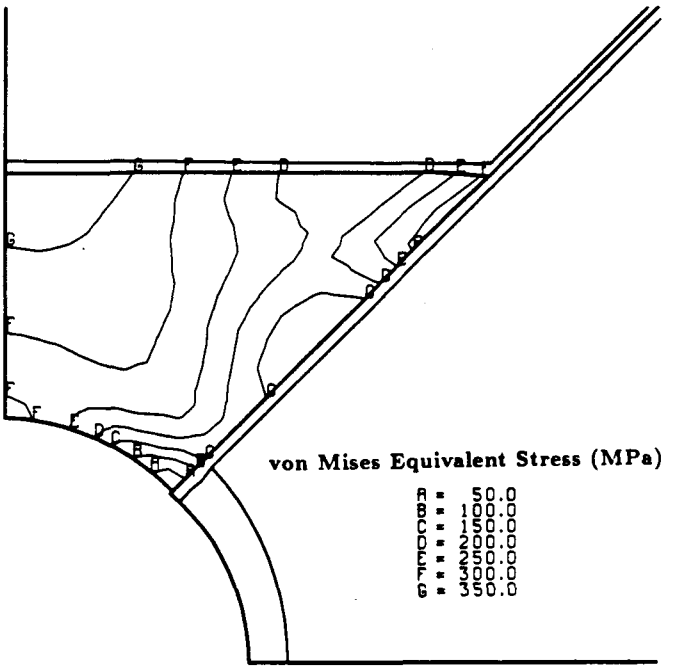

Figure 4.8. Plane-Strain Analysis of Railgun at a Make-up Load of 35 MN/m; von Mises Equivalent Stress contours in GLIDCOP Rail

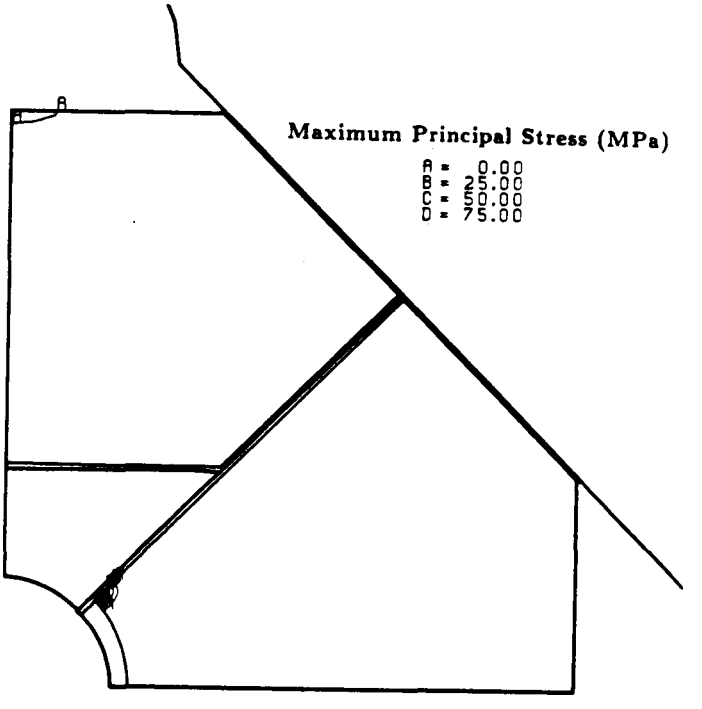

Figure 4.9. Plane-Strain Analysis of Railgun at a Make-up Load of 35 MN/m; Maximum Principal (Tension) Stress Contours in Ceramic Supports

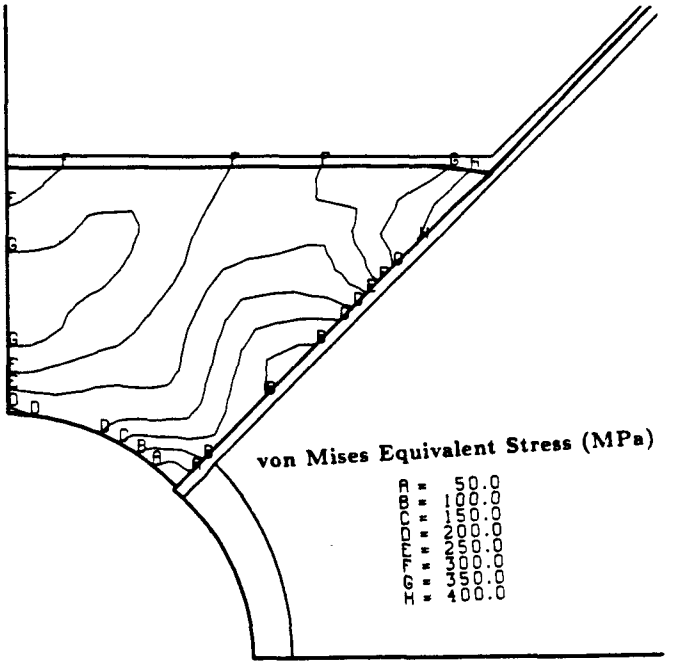

Figure 4.10. Von Mises Equivalent Stress Contours in GLIDCOP Rail at 440 μs for a Rail Current of 600 kA

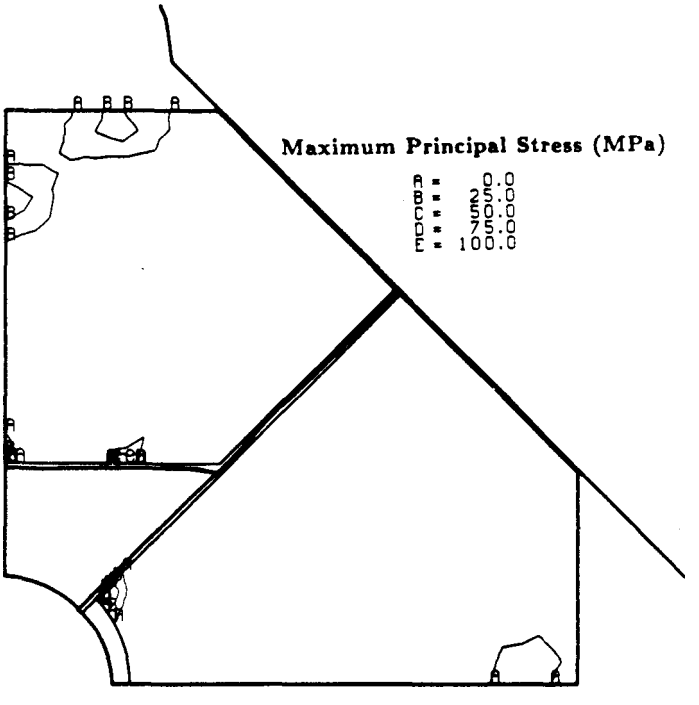

Figure 4.11. Maximum Principal Stress Contours in Ceramic Supports at 460 μs for a Rail Current of 600 kA

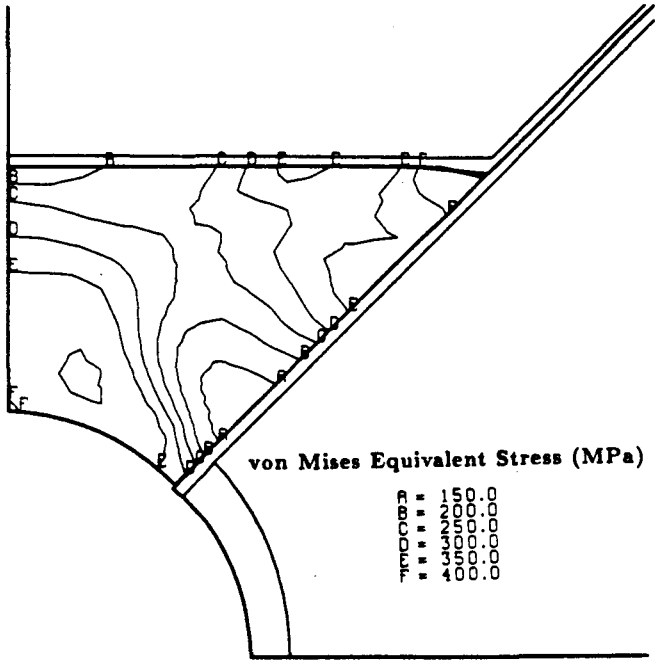

Figure 4.12. Von Mises Equivalent Stress Contours in GLIDCOP Rail at 130 μs for a Rail Current of 700 kA

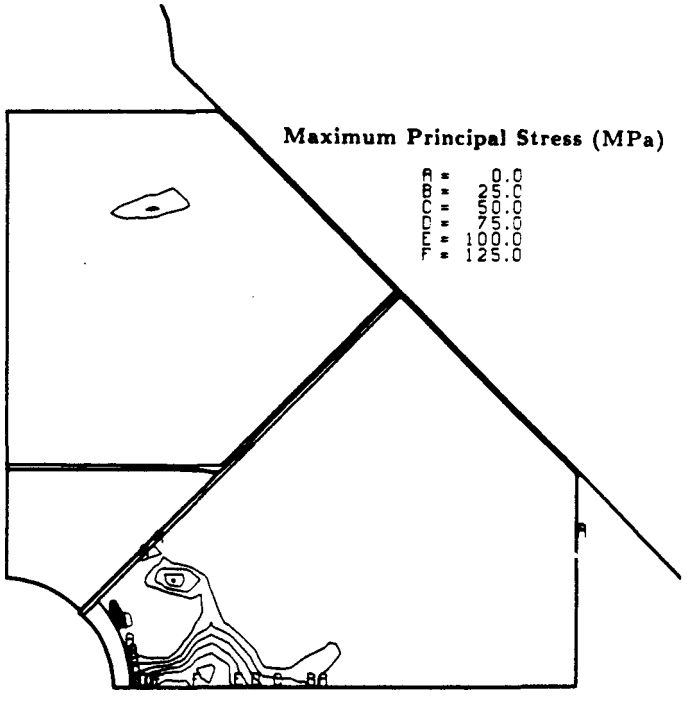

Figure 4.13. Maximum Principal Stress Contours in Ceramic Supports at 130 μs for a Rail Current of 700 kA

almost the entire duration of the operating current application. Significant yielding of the rail at the bore also occurs, as shown in Figure 4.14. Only the ceramic supports behave adequately. The maximum principal stress in the ceramic is 157 MPa at 160 μs into the load cycle, shown in Figure 4.15. This indicates that the maximum operating current of the ceramic core railgun design is limited by the GLIDCOP rail, not the support structure. For this design, the operating current should be restricted to less than 700 kA.

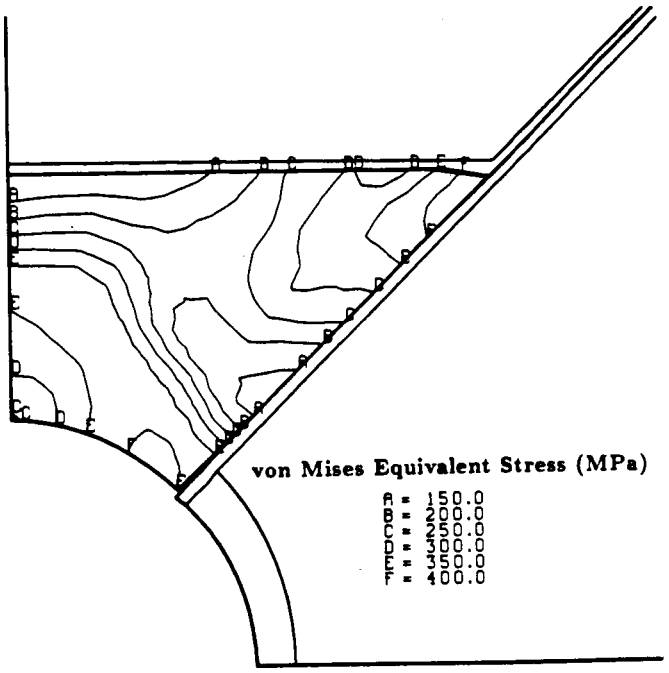

Figure 4.14. Von Mises Equivalent Stress Contours in GLIDCOP Rail at 110 μs for a Rail Current of 800 kA

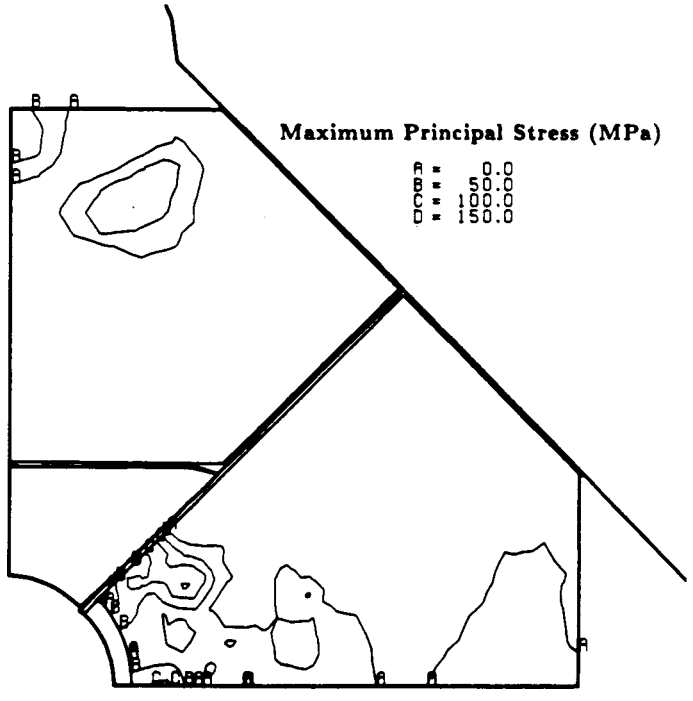

Figure 4.15. Maximum Principal Stress Contours in Ceramic Supports at 160 μs for a Rail Current of 800 kA

5. Conclusions

An evolutionary design process, based on a combination of experiment and analysis, to achieve a high performance railgun structure has been described. The analyses were used to determine stress, strain, and displacement fields of the structure for both the static preload conditions and for the rapidly changing operating loads. The instrumented experiments were used to identify structural failure conditions and to benchmark the analyses.

The railgun structure was evaluated for two criteria; no gap formation at the gun bore during operation, and no failure of any structural components. Model testing revealed that the initial design was subject to cracking of the G-10 insulating supports at a preload of 12 MN/m. Applying a factor of safety, a preload of 8.4 MN/m was selected for the fabrication of the railgun. At this preload, the initial gun design will withstand operating currents of 300 kA and will likely fail under 400 kA operating currents. The introduction of steel trapeziodal supports behind the G-10, suppressed the cracking found in the initial design. This modification allowed the preload to be increased to the full 17 MN/m capacity of the present bolted V-block preloading scheme. With this modification, railgun operation at 500 kA is possible but both bore gaps and G-10 cracking are likely at 600 kA. For future consideration, a replacement of the G-10 with an alumina ceramic was investigated. To take advantage of the higher strength ceramic, a higher preload and thus a new preloading scheme is required. Model tests show that the ceramic can tolerate a preload of at least 51 MN/m. With these modifications, operation at 600 kA is possible. Railgun operation at 700 kA is marginal due to the formation of a narrow short gap at the gun bore. Yielding of the GLIDCOP rail at operating currents above 700 kA limits any further improvements available from design changes in the support structure.

6. References

1. R. S. Hawke, et. al. "STARFIRE: Hypervelocity Railgun Development for High-Pressure Research," IEEE Transactions on Magnetics, Vol. MAG-25, 1989, pp 223-227.

2. G. W. Wellman and K. W. Schuler, "Structural Consequences of Railgun Augmentation," IEEE Transactions on Magnetics, Vol. MAG-25, 1989, pp 593-598.

3. R. S. Hawke, "A Decade of Railgun Development for High Pressure Research," UCRL-99246, Lawrence Livermore National Laboratory, Livermore, California, July 1988.

4. L. M. Taylor and D. P. Flanagan, "PRONTO 2D: A Two-Dimensional Transient Solid Dynamics Program," SAND86-0594, Sandia National Laboratories, Albuquerque, New Mexico, March 1987.

5. T. D. Blacker, "FASTQ User's Manual Version 1.2," SAND88-1326, Sandia National Laboratories, July 1988.

6. L. E. Malvern, *Introduction to the Mechanics of a Continuous Medium*, Prentice-Hall, Inc. Englewood Cliffs, New Jersey, 1969, p. 514.

Distribution:

J. Chase, L-35
R. Hawke, L-35
A. Susoeff, L-373
University of California (3)
Lawrence Livermore Nat. Lab.
P. O. Box 808
Livermore, CA 94550

W. Condit, MS-E526
J. Porter, MS-B218
T. A. Sandford, MS-F618
J. Shaner, MS-J970
Los Alamos National Laboratory (4)
P. O. Box 1663
Los Alamos, NM 87545

Major D. Apo
Major M. Huebsmann
U. S. Army (2)
Innovative Science and Technology Office
The Pentagon
Washington, DC 20301-7100

D. Littrel
A. Young
A.F.A.T.L./S.A.H. (2)
Okaloosa Island
Eglin A.F.B., FL 32542-5434

I. McNab
Westinghouse Electric Corp. (1)
P. O. Box 499
401 E. Hendy Avenue (MS 92-20)
Sunnyvale, CA 94088

Lt.-Col. E. Mertz
Major P. Rustan
U. S. Air Force (2)
R.A.E.V.
Defense Nuclear Agency
Washington, DC 20305

J. Gagliano
Air Force Armament Lab. (1)
Eglin A.F.B., FL 32542

W. M. Isbell
Effects Technology (1)
5383 Hollister Ave.
Santa Barbara, CA 93111

F. Jamet
French-German Research Institute (ISL) (1)
Saint Louis, France

R. Dethlefsen
Maxwell Laboratories (1)
8888 Balboa St.
San Diego, CA

W. J. Kolkert
Prins Mauritz Lab. TNO (1)
P. O. Box 45
2280 AA Ryswyk
The Netherlands

A. B. Sawaoka
Tokyo Institute of Technology (1)
Midori, Yokohama 227
Japan

Hideaki Kashii
TRDI, Japan Defense Agency (1)
2nd Div., 1st Research Center
2-2-1 Nakameguro, Neguro-kn
Tokyo, 153 Japan

H. F. Swift
Physics Applications, Inc (1)
800 Britton Road
Dayton, OH 45429

N. K. Winsor
GT-Devices, Inc. (1)
5705 General Washington Dr.
Alexandria, VA 22312-2408

R. Zowarka
University of Texas (1)
Center for Electromechanics
10100 Burnet Road
Austin, TX 78758

Sandia Internal:

1130 G. A. Samara
1131 B. Morosin
1131 M. B. Boslough
1200 J. P. VanDevender
1220 M. Cowan
1221 M. M. Widner
1241 J. R. Freeman
1241 R. S. Coats
1510 J. W. Nunziato
1520 L. W. Davison
1521 L. W. Davison, actg.
1521 G. W. Wellman (15)
1522 R. C. Reuter
1522 K. W. Schuler
1523 J. H. Biffle
1524 D. R. Martinez
1530 D. B. Hayes
1531 C. Westmoreland
1533 F. R. Norwood
1534 J. R. Asay (5)
1534 L. M. Barker
1534 L. C. Chhabildas
1534 J. E. Dunn
1534 C. Hall
1534 M. Shahinpoor
1534 C. H. Konrad
1534 R. D. Hardy
1550 C. W. Peterson
1831 J. W. Munford
1832 W. B. Jones
1832 R. J. Bourcier
1845 F. P. Gerstle, Jr.
3141 S. A. Landenberger (5)
3151 W. I. Klein (3)
3141-1 C. L. Ward (8)
for DOE-OSTI
5160 G. R. Otey
5160 J. F. Cuderman
5248 D. W. Hannum
7530 T. L. Workman
7531 D. R. Schafer
7535 D. C. Bickel
7540 T. B. Lane
7542 T. G. Priddy
7542 R. A. May
7542 L. R. Dorrell
8400 R. C. Wayne
8524 J. A. Wackerly
9010 W. C. Hines
9120 M. M. Newsom
9122 R. O. Nellums
9130 R. D. Andreas
9140 D. J. Rigali
9142 W. J. Tedeschi